SANDIA REPORT

SAND2016-10750
Unlimited Release
Printed September, 2016

Improved Mechanical Performance, Fracture Properties, and Reliability of Radical-Cured Thermosets

Erica M. Redline, Dan S. Bolintineanu, J. Matthew D. Lane, Mark J. Stevens, Todd M. Alam, Mathias C. Celina

Prepared by
Sandia National Laboratories
Albuquerque, New Mexico 87185 and Livermore, California 94550

Sandia National Laboratories is a multi-mission laboratory managed and operated by Sandia Corporation, a wholly owned subsidiary of Lockheed Martin Corporation, for the U.S. Department of Energy's National Nuclear Security Administration under contract DE-AC04-94AL85000.

Issued by Sandia National Laboratories, operated for the United States Department of Energy by Sandia Corporation.

Available to DOE and DOE contractors from
U.S. Department of Energy
Office of Scientific and Technical Information
P.O. Box 62
Oak Ridge, TN 37831

Telephone: (865) 576-8401
Facsimile: (865) 576-5728
E-Mail: reports@adonis.osti.gov
Online ordering: http://www.osti.gov/bridge

Available to the public from
U.S. Department of Commerce
National Technical Information Service
5285 Port Royal Rd
Springfield, VA 22161

Telephone: (800) 553-6847
Facsimile: (703) 605-6900
E-Mail: orders@ntis.fedworld.gov
Online ordering: http://www.ntis.gov/help/ordermethods.asp?loc=7-4-0#online

SAND2016-10750
Unlimited Release
Printed September, 2016

Improved Mechanical Performance, Fracture Properties, and Reliability of Radical-Cured Thermosets

Erica M. Redline, Dan S. Bolintineanu, J. Matthew D. Lane,
Mark J. Stevens, Todd J. Alam, and Mathias C. Celina

Abstract

The aim of this study was to alter polymerization chemistry to improve network homogeneity in free-radical crosslinked systems. It was hypothesized that a reduction in heterogeneity of the network would lead to improved mechanical performance. Experiments and simulations were carried out to investigate the connection between polymerization chemistry, network structure and mechanical properties. Experiments were conducted on two different monomer systems - the first is a single monomer system, urethane dimethacrylate (UDMA), and the second is a two-monomer system consisting of bisphenol A glycidyl dimethacrylate (BisGMA) and triethylene glycol dimethacrylate (TEGDMA) in a ratio of 70/30 BisGMA/TEGDMA by weight. The methacrylate systems were crosslinked using traditional radical polymerization (TRP) with azobisisobutyronitrile (AIBN) or benzoyl peroxide (BPO) as an initiator; TRP systems were used as the control. The monomers were also cross-linked using activator regenerated by electron transfer atom transfer radical polymerization (ARGET ATRP) as a type of controlled radical polymerization (CRP). FTIR and DSC were used to monitor reaction kinetics of the systems. The networks were analyzed using NMR, DSC, X-ray diffraction (XRD), atomic force microscopy (AFM), and small angle X-ray scattering (SAXS). These techniques were employed in an attempt to quantify differences between the traditional and controlled radical polymerizations. While a quantitative methodology for characterizing network morphology was not established, SAXS and AFM have shown some promising initial results. Additionally, differences in mechanical behavior were observed between traditional and controlled radical polymerized thermosets in the BisGMA/TEGDMA system but not in the UDMA materials; this finding may be the result of network ductility variations between the two materials. Coarse-grained molecular dynamics simulations employing a novel model of the CRP reaction were carried out for the UDMA system, with parameters calibrated

based on fully atomistic simulations of the UDMA monomer in the liquid state. Detailed metrics based on network graph theoretical approaches were implemented to quantify the bond network topology resulting from simulations. For a broad range of polymerization parameters, no discernible differences were seen between TRP and CRP UDMA simulations at equal conversions, although clear differences exist as a function of conversion. Both findings are consistent with experiments. Despite a number of shortcomings, these models have demonstrated the potential of molecular simulations for studying network topology in these systems.

Acknowledgments

The authors would like to thank Greg O'Bryan, Nicholas Giron, Adam Quintana, Charles E. Harris, Ana Trujillo, Mark Rodriguez, Jamie Stull, Ross Muenchausen, Darren Dunphy, Cassandria Miller, Patti Sawyer, Mark Stavig, and Gabriel Arechederra for experimental and/or analytical assistance.

Contents

Appendix

List of Figures

List of Tables

Chapter 1

Introduction

Thermosets are crosslinked polymers which are commonly used in applications that require a high modulus and good chemical and thermal stability [41]. Many industries such as automotive, aeronautical, construction, and electrical use thermoset materials in structural or protective functions due to their favorable properties. Thermosets are typically classified by the way they are polymerized, i.e. step- or chain-growth. In a step-growth polymerization, networks are built up by the stepwise addition of monomers and the reaction ends when all of the monomer has reacted with one another; a typical example of this type of material is an epoxy. A chain-growth polymerization occurs by the initiation of an active site where monomers are rapidly added in a step called propagation. Polymerization only transpires through active centers, with a rapid molecular weight build up relative to step-growth polymerization. The reaction is ended by termination of the active sites, which can happen through various mechanisms. Vinyl esters, unsaturated polyesters and methacrylates are all crosslinked using this chemistry [4, 12, 40].

One drawback of thermoset polymers is that the high degree of crosslinking also makes the materials very brittle and prone to fracture. Thus, a significant effort has been undertaken in order to improve toughness and fracture properties of thermosets. The most common strategy for toughening involves the use of a secondary phase such as rubber particles, inorganic nanoparticles, homopolymers, dendrimers, and amphiphilic block copolymers [2, 20, 35, 49]. While the incorporation of a secondary phase works well in toughening step-polymerized thermosets, it has not been as successful with chain polymerized systems [45]. It was speculated that step-growth thermosets are generally more robust and easier to toughen than chain polymerized thermosets due to improved network regularity afforded by the step polymerization chemistry [45]. In fact, chain-growth thermosets are known to form heterogeneous networks which tend to have many defects such as loops and dangling ends [6, 28, 47].

While efforts to improve toughness of chain polymerized thermosets have focused primarily on the additive strategy, only a few studies looked at enhancing network regularity [26, 29, 60]. Of those studies which focused on network formation, all used a form of controlled radical polymerization (CRP). CRP is a type of chain polymerization in which termination and transfer reactions are (ideally) eliminated by the reversible activation/deactivation of propagating radical species. There are three primary categories of CRP based on the chemistry involved: nitroxide mediated (NMP) [39], reversible addition-fragmentation chain transfer (RAFT) [37], and atom transfer radical polymerization (ATRP) [34, 54]. Since

radical species are kept primarily in a dormant state, tight control over molecular weight, molecular weight distribution, and polymer architecture is possible [42]. These types of polymerizations are primarily used in the solution state and have sparingly been investigated in bulk polymerizations to form crosslinked networks.

Ide and Fukuda [25, 26] were some of the first to use controlled radical polymerization in a crosslinked system. The authors used both traditional and nitroxide-mediated polymerization to copolymerize vinyl and divinyl monomers in an effort to evaluate pendant vinyl group reactivity [25] and gelation [26]. Their initial interest was to reduce the amount of intramolecular crosslinks which form cycles and do not add to the molecular weight of the network. These cyclization reactions create one to two orders of magnitude difference between the critical number of crosslinks at the gel point determined experimentally versus what is predicted theoretically [13, 14, 15, 16, 50, 51]. The authors further showed that gels prepared using a traditional radical polymerization contained microgels at very low conversions (<0.05) whereas microgels were not observed in the NMP system until the critical conversion of monovinyl monomer at the gel point was reached. Furthermore, overall gel content and swelling ratio of the materials indicated that the network formed by the NMP reaction was more homogeneous than the TRP cured system and the critical number of crosslinks at the gel point agreed within a factor of two between experiment and theory for the NMP system [25, 26].

Yu et al. [59] investigated the polymerization of polyethylene glycol dimethacrylate (PEGDMA) using ATRP. By monitoring the reactions of ATRP using electron spin resonance, the authors were able to uncover that the ATRP reaction proceeded in a living manner until approximately 40% conversion, after which point increased viscosity slowed diffusion of the catalyst/ligand complex, causing an increase in radical concentration and the reaction to progress in a traditional fashion. In a follow-up paper, Yu and coworkers [60] used ATRP and TRP to synthesize crosslinked networks of PEGDMA with varying starting molecular weights. The authors found that the ATRP sample had a final cure of 87.5% while the TRP sample was 96.3%. The rate of reaction for the ATRP was considerably slower, taking approximately 80 minutes to reach final cure state while the TRP sample was cured in 20 minutes. Dynamic mechanical analysis (DMA) of the network showed a broader peak in tan δ of the TRP-cured versus ATRP sample. The authors suggested that peak width of tan δ could be used as a means to investigate network heterogeneity; the narrower the tan δ peak, the more homogeneous the network. It was also discovered that decreasing initial PEGDMA molecular weight led to increased heterogeneity, which was attributed to a higher local concentration of pendant double bonds; the higher concentration of pendant double bonds thus increased the probability of microgel formation.

Jiang and coworkers [29] also used ATRP in the copolymerization of two dimethacrylate monomers to create hydrogels. The paper noted an acceleration in polymerization rate at high conversions, which the authors believed to be due to the metal-ligand complex reactions becoming diffusion controlled. In addition, the authors noted a mere factor of five difference in the experimental gel point versus the theoretical gel point calculated using Flory's theory [16] in the ATRP-cured system. Again, this theory assumes a homogeneous

network, with conventional radical polymerizations deviating from theory by an order of magnitude or more [26]. Thus, the authors concluded that the ATRP-cured material had a more homogenous network based upon the closer proximity of the experimental gel point in relation to the theoretically-derived gel point.

In another study, Ward et al. [55] observed the kinetics of a living radical polymerization of multifunctional monomers using an iniferter (a molecule that acts as initiator, transfer agent, and terminator all at once) and UV light rather than a thermally-induced cure, as in the previously mentioned papers. It was found that the rate of polymerization was significantly decreased in the presence of the iniferter used in the living reaction versus a conventional UV-cured reaction. Furthermore, autoacceleration of the reaction, which is common in traditional radical polymerizations, did not occur in the living polymerization case. The initial living cure lead to low conversions, but this could be improved by increasing the amount of iniferter, light intensity, and/or temperature. Finally, the authors used tan δ as a probe of network heterogeneity and found that the iniferter-cured system did not have an effect on the heterogeneity - it just slowed down the reaction rate; the inability to change network structure using a controlled polymerization was attributed to the pendant double bond reactivity being unaffected by the iniferter. These results are contrary to the thermally cured systems, where CRP was shown to reduce network heterogeneity [25, 26, 59, 60, 29].

One major drawback of using CRP is that the chemistry is sensitive to moisture and oxygen, which would make using this method of crosslinking challenging for many of the chain polymerized thermosets. ATRP tends to be less prone to these impurities and recent advances in ATRP, such as activator regeneration by electron transfer (ARGET) ATRP, have been shown to be even less sensitive. ARGET ATRP has the additional advantage of being considered a "green" polymerization method because it requires a much lower concentration of metal catalyst (typically a copper complex) than other forms of ATRP [42]. For these reasons, ARGET ATRP was chosen as the CRP system for this research project.

Despite the importance of controlled radical polymerization (CRP) schemes such as ARGET ATRP, relatively few studies have attempted to carry out molecular simulations of CRP mechanisms. Typical modeling efforts employ continuum kinetic models that capture the time evolution of the concentrations of different species. Both deterministic [38, 21, 62, 61] and stochastic models of chain growth [23] have been successfully fit to experimental data in order to identify reaction mechanisms and measure kinetic parameters in CRP. For a recent survey of literature in this area, the interested reader is referred to the review by Mastan et al [36]. In this work, we are interested in structural features of crosslinked networks at length scales comparable to the molecular scale; continuum approaches are therefore not applicable, as they do not yield information regarding network structure. At the opposite end of the length scale spectrum, explicit atomistic simulations of reacting molecules must account for electronic degrees of freedom involved in the formation of bonds and activation/deactivation of free radicals. The most rigorous treatment of these effects requires quantum mechanical simulations (e.g. ab-initio molecular dynamics [22, 11]), or reactive force fields (e.g. REAX-FF [52, 7]). Due to the computationally intensive nature of such treatments, their use for network-scale simulations is currently prohibitive. We therefore

employ a coarse-grained molecular dynamics approach that is intermediate in length and structural detail between the atomistic and continuum scales. Comparable approaches include lattice-based models [19, 17] or dissipative particle dynamics (DPD) approaches with reactive sites [58, 57]. However, to our knowledge, the model we develop here is the first molecular dynamics approach that includes the effects of radical activation and deactivation for a CRP mechanism.

The focus of this study is to provide a unique approach to understanding how network homogeneity impacts mechanical performance of thermoset polymers by merging both experimental and theoretical techniques. While there is already experimental evidence that using CRP leads to more homogeneous networks, the amount of heterogeneity has yet to be quantified and compared to traditional radical polymerizations. In addition, ARGET ATRP has yet to be investigated for its efficacy in reducing network heterogeneity. Our theoretical approach utilizes coarse grained simulations informed by atomistic simulations to generate crosslinked polymer structures using a realistic polymerization scheme. The level of structural detail in these simulations enables us to quantify and explore network structure as a function of various polymerization parameters.

Chapter 2

Materials and Methods

Materials

Urethane dimethacrylate (UDMA) and a 70/30 w/w mixture of bisphenol A glycidyl meth-acrylate(BisGMA)/triethylene glycol dimethacrylate (TEGDMA) were donated by Esstech, Inc. (Essington, PA) and used as received. Figure 2 shows the chemical structures of these monomers. Azobisisobutyronitrile (AIBN), benzoyl peroxide (BPO), copper (II) chloride, tin (II) 2-ethylhexanoate ($SnII[Eh]_2$), ethyl α-bromoisobutyrate (EαIBr), and tris[2-(dimethylamino)ethyl]amine (Me_6Tren) were purchased from Sigma-Aldrich and also used as received.

Experimental Methods

Traditional radical polymerization

Traditional radical polymerizations (TRP) were conducted by mixing 1 wt. % of BPO or AIBN with the BisGMA/TEGDMA blend or UDMA. The mixture was then heated to 40 °C (AIBN), or 75 °C (BPO) and stirred on a hot plate for approximately 5 minutes to incorporate the initiator. The materials were de-gassed at 40 °C for 10 minutes and poured into a silicone mold to create rectangular bars of 2.5 in. length, 0.5 in. width and 0.25 in. thickness. Approximately 5 g of material was needed to fill each rectangular mold. Samples were placed into a vacuum oven where they underwent two cycles of vacuum/purge with N_2 before being heated to the cure temperature, 70, 80, or 90 °C, and cured for 20 hrs. In some cases, materials were post-cured at 150 °C for two hours to promote additional curing.

Controlled Radical Polymerization

Activator regenerated by electron transfer atom transfer radical polymerization (ARGET ATRP) was employed for the controlled radical polymerizations (CRP). This method was chosen over other radical polymerizations as it is much less sensitive to oxygen and water

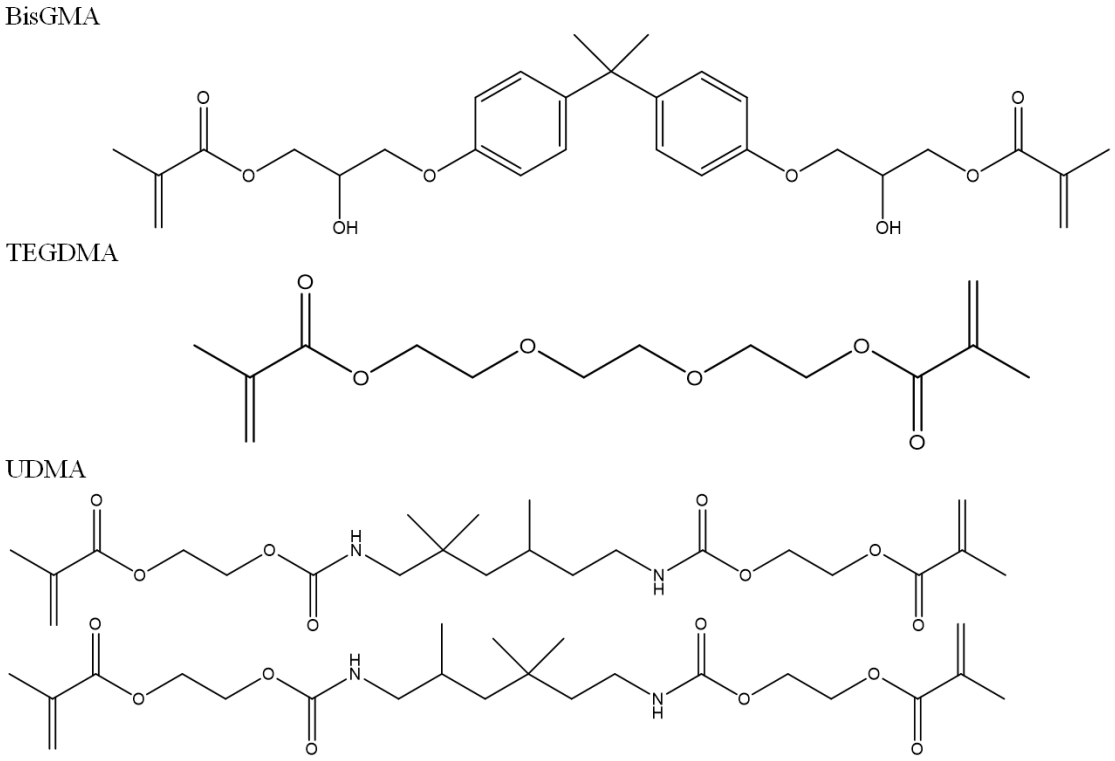

Figure 2.1. Chemical structures of the monomers used in this study.

impurities. For this reaction, copper (II) chloride was used as the metal halide, tin (II) 2-ethylhexanoate was employed as a reducing agent, ethyl α-bromoisobutyrate as the initiator, and tris[2-(dimethylamino)ethyl]amine as the ligand. Samples were prepared in a molar ratio of 160: 1: 0.1: 0.1: 0.01 methacrylate groups: initiator: reducing agent: metal halide. Materials were mixed on a hot plate at 40 °C, de-gassed in a vacuum oven of the same temperature, then poured into a mold, pump/purged twice, and cured as described in Section 2. Curing temperatures were 70, 80, or 90 °C. In some cases, materials were post-cured to 150 °C for two hours to promote additional curing.

Cure Kinetics

Attenuated Total Reflection Fourier Transform Infrared Spectroscopy(ATR FTIR)

ATR FTIR was carried out on a Bruker Equinox 55 spectrometer with a DTGS (ID301/8) detector operating at RT and a Pike GladiATR diamond ATR single reflection crystal. Spectra were averaged over 32 scans at a 4 cm^{-1} resolution over a 4000-500 cm^{-1} scanning range. A calibration curve was made for each monomer system whereby a known concentration of the monomer was mixed with an epoxy, Heloxy-8; this particular epoxy monomer was chosen as it had no IR signal around the 1637 cm^{-1} band associated with the methacrylate group of the monomers. Spectra were taken at regular intervals throughout the cure, and the area under the 1637 cm^{-1} band calculated. These data were compared to the calibration curve to obtain the extent of cure as a function of time.

Nuclear Magnetic Resonance (NMR)

NMR was performed as a secondary verification of extent of cure as well as to determine the composition of the sol fraction of the cured materials. Solution NMR spectra were obtained on a Bruker Avance III 500 instrument using a 5 mm broadband probe with standard 1H and 13C pulse sequence conditions. The starting monomer compound was dissolved in DMSO, with the 1H and 13C chemical shift referenced to solvent signal with respect to TMS $\delta = 0$ ppm.

The solid state NMR was performed on a MAS NMR Bruker Avance III 600 NMR instrument using a 4 mm rotor spinning at 10 kHz. The 1D 13C MAS NMR spectra were obtained using standard CP conditions with a 1 ms recycle delay. In addition, one pulse Bloch decay were obtained to address relative concentrations. The 13C NMR chemical shifts were referenced to the secondary external standard glycine, with the carbonyl resonance δ = 176.0 ppm with respect to TMS $\delta = 0$ ppm.

Differential Scanning Calorimetry (DSC)

Measurements were carried out using a TA Instruments Q200 differential scanning calorimeter. Approximately 20 mg of material was placed in an aluminum pan without a lid, heated rapidly (c.a. 50 °C/min) to the isothermal cure temperatures of 70, 80, or 90 °C, and held for seven to twenty hours. Then, samples were ramped to 150 °C and held for two hours before being quenched to room temperature. During the test, an N_2 purge of 50 mL/min was used to prevent oxygen inhibition of curing in the ATRP samples.

Conversion, C, was determined using the following equation:

$$C = \Delta H_t / \Delta H_0^{theor} \tag{2.1}$$

and polymerization rate, R_p, by:

$$R_p = \frac{\frac{dH}{dt}}{\Delta H_0^{theor}} \tag{2.2}$$

where ΔH_t is the heat of reaction released to time t, $\Delta H_0{}^{theor}$ is -54.4 kJ/mol for methacrylates [46], and $\frac{dH}{dt}$ is the heat flow.

Mechanical Properties

Thermosets were molded into bars of approximately 64 x 12 x 4 mm, and surfaces polished prior to testing to ensure sample dimensions were as even as possible. Stress and strain at break as well as modulus were determined for the crosslinked materials using an Instron 5500R in a three-point bend configuration with a two inch span. A test rate of 2 mm/min was used until failure or until the sample reach 10 mm extension, at which point the sample was severely bowed and slipping from the grips. Flexural modulus was calculated from the slope of the linear portion of the stress-strain curve.

Network Analysis

Differential Scanning Calorimetry (DSC)

Differential scanning calorimetry, DSC, was employed to measure the glass transition temperature, T_g of the cured materials. Approximately 10 mg of material were sealed in aluminum pans and placed in a TA Instruments Q2000 DSC. The temperature was ramped from 0 to 200 °C twice at 10 °C/min and T_g determined from the second cooling curve.

Nuclear Magnetic Resonance (NMR)

See solution state NMR details listed above under Cure Kinetics.

Solvent Uptake and Gel Content

Solvent uptake and gel content measurements were conducted by placing samples in refluxing cyclohexane or cyclohexanone for approximately 50 hours followed by drying at room temperature overnight and an additional drying step at 150 °C until constant mass was achieved. The solvent uptake factor was calculated as the mass of the swelled sample divided by the initial mass of the sample ($m_{swelled}/m_i$) and gel content by dividing the mass of the dried sample by the initial sample mass (m_{dried}/m_i).

Atomic Force Microscopy (AFM)

A Dimension Icon atomic force microscope was used in tapping mode with a TESPA tip having nominal tip radius of 8 nm. Images of cured materials were scanned with a 300 nm scan size at a rate of 0.5 Hz.

X-ray Diffraction (XRD)

XRD was performed on using CuKα radiation with wavelength = 0.154184 nm. Particle size, D, was calculated using the Scherrer equation:

$$D = \frac{k\lambda}{\beta_D \cos\theta} \tag{2.3}$$

where k is the constant depending upon lattice direction and crystallite morphology ($k = 1$), λ is the wavelength of radiation (0.154184 nm), β_D is the full width at half maximum intensity of the scattering peak, and θ is the scattering angle between the transmitted and diffracted radiation [48].

Small Angle X-ray Scattering (SAXS)

Small angle X-ray scattering was carried out at the Advanced Materials Laboratory to look for differences in the network morphology on length scales of around 10 - 150 nm.

Molecular dynamics simulations

In coarse-grained (CG) molecular dynamics simulations, molecules are represented using simple bead-spring models. Each bead, or site, represents a group of atoms. During the course of the simulations, bonds are formed between certain sites to simulate the key reaction steps, as described in more detail below. We use a relatively simple scheme to represent the ATRP reaction mechanism in order to minimize the number of simulation parameters, many of which cannot easily be determined experimentally. Similar approaches have been successfully used in modeling epoxy network formation in atomistic simulations [56], but these are typically limited to generating initial configurations rather than simulating dynamics that resemble a polymerization reaction. Heine and coworkers carried out atomistic simulations of end cross-linked poly(dimethylsiloxane) (PDMS) using a probabilistic bond formation model to capture dynamic network formation [24]. We adopt a conceptually similar strategy here, with the only additional complication due to the ATRP mechanism, which requires dynamically evolving reactive sites. To the best of our knowledge, this is the first molecular dynamics simulation of a polymer system formed via ATRP that accounts for radical activation/deactivation. While an atomistic variant of this approach may also be feasible for these systems using a non-reactive force field (e.g. OPLS [32]), the lack of force field parameters, computational limitations, and uncertainty in reaction mechanisms do not justify the additional simulation complexity. A coarse-grained approach also allows for more rapid exploration of the parameter space, as well as larger domain sizes that capture long-range structural features of the cross-linked polymer network. However, we do use atomistic simulations of the monomers (see section 2) to calibrate intramolecular parameters in the CG model.

Coarse-grained model of UDMA

We have focused our simulation efforts on the UDMA system, as it requires less parameter calibration due to the presence of a single monomer species. However, the same methods could also be applied to the BisGMA/TEGDMA system. Preliminary proof-of-concept simulations were carried out using a five-site model of UDMA, where all sites and intramolecular bonds were identical. Atomistic simulations of the monomer melt system then suggested the potential importance of monomer flexibility characteristics to network formation (e.g. "back-biting" reactions). We therefore moved to a more sophisticated seven-site model, with intramolecular bond parameters calibrated based on atomistic simulations. The mapping between the atomistic and coarse-grained representation is shown in figure 2.2. Each site in the coarse-grained representation is treated as a Lennard-Jones particle with mass set equal to the sum of the masses of the atoms it represents. All CG simulation quantities are reported in reduced units, where the mass unit is set to the mass of the type 1 site (i.e. a mass of 1 is equivalent to 69.08 a.m.u.) and the length unit is the length of the site 1- site 2 equilibrium bond length (3.6 $\AA$). The non-bonded interaction energy $U(r)$ between two sites separated by distance r is:

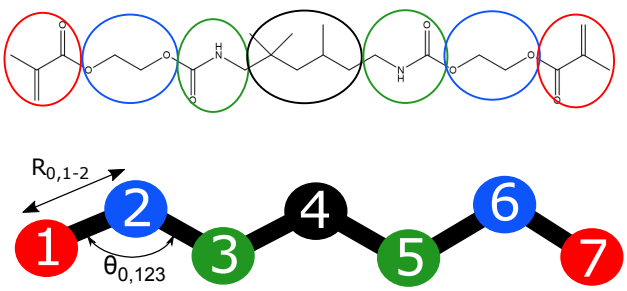

Figure 2.2. Coarse-grained model of UDMA. Top: the chemical structure of UDMA. Bottom: the coarse-grained bead-spring representation of UDMA, including site numbers referenced in tables 2 and 2. Examples of bond and angle energy terms are also depicted.

$$U(r) = 4\epsilon\left(\left(\frac{\sigma}{r}\right)^{12} - \left(\frac{\sigma}{r}\right)^{6}\right) \tag{2.4}$$

Here, ϵ and σ are the usual Lennard-Jones parameters that control the energy and length scale of the non-bonded interaction. The interaction energy ϵ is used as the unit of energy. The reduced time units are then $\tau = \sqrt{\epsilon/m\sigma^2}$ We include harmonic bonded interactions between sites separated by a single bond ($U(R) = k_b(R - R_0)^2$, where k_b controls the bond stiffness and R_0 is the equilibrium bond length); and harmonic angle interactions between sites separated by two bonds ($U(\theta) = k_\theta(\theta - \theta_0)^2$, where θ is the angle formed by the three sites involved, k_θ is the angle stiffness parameter, and θ_0 is the equilibrium angle value). Non-bonded interactions (equation 2.4) are turned off for pairs of sites that interact via bond or angle terms.

The equilibrium values R_0 and θ_0 for bonds and angles are obtained directly from averages of these quantities for the corresponding geometries in atomistic simulations. In all cases, the centers of mass of the group of atoms that represent a given site are used to compute the separation or angle between groups. The stiffness values k_b and k_θ are set based on the fluctuations in R_0 and θ_0; as these are equilibrium values in an NVT ensemble, they follow the Boltzmann distribution:

$$P(R_0) \propto \exp(-U(R_0)/T) = \exp(-k_b(R - R_0)^2/T) \tag{2.5}$$

Here, T is the thermal energy scale (equivalent to the Lennard-Jones temperature, which we choose to be 0.8, as described below). The right hand term in equation 2.5 is simply a Gaussian distribution with mean R_0 and standard deviation given by:

$$\sigma_{R_0} = \sqrt{2T/k_b} \tag{2.6}$$

Table 2.1. Intramolecular bond parameters for CG simulations. Length units are scaled based on the site 1 - site 2 mean separation distance of $3.6\mathring{A}$. Refer to figure 2.2 for site numbers.

Bonded sites	$k_b(\epsilon/\sigma^2)$	$R_0/R_{0,1-2}$
1-2	128.44	1
2-3	98.61	0.9658
3-4	49.55	1.064
4-5	27.60	1.235
5-6	99.61	0.9700
6-7	141.45	1.003

Table 2.2. Intramolecular angle parameters for CG simulations. Refer to figure 2.2 for site numbers.

Bonded sites	$k_\theta(\epsilon/\text{rad}^2)$	θ_0 (deg.)
1-2-3	1.970	132.75
2-3-4	5.227	131.52
3-4-5	1.428	100.59
4-5-6	3.725	134.73
5-6-7	2.078	134.22

We therefore use the atomistic simulations to measure the standard deviation σ_{R_0} of the separation length between each pair of bonded sites. The bond stiffness k_b specific to each pair of sites is then computed by re-arranging equation 2.6. A completely analogous procedure is used to obtain k_θ values for all angle interactions, where the standard deviation of the angle values is again obtained from atomistic simulations. Tables 2 and 2 summarize the key bonded parameters used in the CG simulations as obtained using the atomistic simulations.

As for the non-bonded interaction parameters ϵ and σ in equation 2.4, we set them to unity for all particle types for simplicity; a more sophisticated approach (e.g. inverse-Boltzmann mapping using radial distribution functions) was considered, but deemed too cumbersome due to the relatively large number of combinations of pairwise interactions between different site types.

ATRP polymerization model

We use a probabilistic bond formation model to capture the key features of the ATRP process. As in the case of the experiments, the reaction proceeds from a liquid of monomer molecules. Monomers are initially placed in the gas state with their centers of mass on a large simple cubic lattice, and allowed to equilibrate and condense via a constant pressure and temperature simulation in a 3D-periodic simulation box. The equilibration stage is

considered complete when the system volume reaches a constant value, which typically only requires $\approx 3 \times 10^5$ time steps. All simulations discussed here were carried out at a dimensionless temperature of $T = 0.8$, which was found to exceed the simulation T_g value of the monomer melt (see section 3).

The model requires particle types to change during the course of the simulation according to a set of simple reaction rules. For purposes of the reaction scheme, we designate end groups as simply type 1 if they are inactive and unreacted. End groups that are active radicals are designated type 2, end groups that are protected/dormant due to ligand binding are designated type 3, and end groups that have reacted are designated type 4. Note that this is a completely different numbering scheme than that used in figure 2.2 for purposes of assigning bonded parameters (sites 1 and 7 in figure 2.2 are assigned a site type 1-4 depending on their reaction state as just described; sites 2-6 in figure 2.2 do not play a role in the reaction).

An important feature of the model is that both the initiator and catalyst are represented implicitly rather than using additional particles. For the case of the initiator, this simply involves setting a prescribed fraction of type 1 particles to active (type 2) or dormant (type 3) radical groups. In the simulations, this takes place at a single time point following equilibration, and marks the start of the CRP reaction. This approach effectively ignores the first initiator-monomer binding event for each chain, and instead treats only the resulting activated monomers. We do not consider this to be a relevant shortcoming of the model, since the initiator molecule will only have a minor effect on the local structure near the start of a chain, and these are extremely small regions compared to the rest of the system. The fraction of type 1 particles that are changed to type 2 or type 3 particles at the start of the polymerization simulation is denoted as x_i, and represents the initiator:reactive site ratio:

$$x_i = \frac{N_2 + N_3}{N_1 + N_2 + N_3} \tag{2.7}$$

Among particles that are initially changed from type 1 to types 2 or 3 (i.e. initiated), the ratio between particles that are changed to type 2 (active radicals) and the total that are changed to type 2 or type 3 (any type of radicals) is denoted as K_a, and effectively represents the equilibrium constant of the ATRP activation/deactivation reaction (strictly speaking, the equilibrium constant K_{eq} of the reaction is the ratio of active to dormant radicals, so that $K_{eq} = K_a/(1 - K_a)$. We use K_a here for simplicity):

$$K_a = \frac{N_2}{N_2 + N_3} \tag{2.8}$$

The effect of the catalyst is also modeled implicitly by randomly switching the states of active/dormant radicals (i.e. switching particles of type 2 to type 3 and vice versa). During the course of the simulation, particles of type 2 and type 3 are considered individually at prescribed intervals, and regardless of their current state, are set to particles of type 2

with probability K_a, and to particles of type 3 with probability $1 - K_a$. This means that on average the fraction of active radicals among all radicals is K_a, as is the case for the initial state of the system. Controlled radial polymerization (CRP) corresponds to relatively small values of K_a (i.e. $K_a \ll 1$), whereas for $K_a = 1$ we recover a traditional radical polymerization (TRP) scheme. The frequency at which the activation/deactivation attempts take place is an additional parameter N_a that specifies a number of simulation time steps between attempts. Clearly, this scheme is an approximation of a much more complex series of events. In reality, the unbinding of the catalyst results in the transition from dormant to active radicals (activation), and binding of the catalyst to the ligand/metal complex; the catalyst/metal-ligand complex then diffuses, and eventually binds to another radical to deactivate it, releasing the metal-ligand complex in the process. By omitting an explicit representation of the catalyst, the model potentially fails to capture spatial correlations in activation/deactivation of radicals, as well as possible differences in binding of the catalyst arising from local differences in cross-link density (i.e. local differences in viscosity, which would lead to slower catalyst diffusion). However, in the regime where the time scales associated with diffusion of the catalyst are much faster than the reaction kinetics, these effects are not expected to be significant. Furthermore, including an explicit representation of the catalyst leads to a significant increase in simulation complexity, and the need for additional parameters and mechanisms that are not well characterized. More sophisticated models that include the catalyst and metal/ligand complex explicitly are recommended for future work in this area.

The chain elongation step of the polymerization is modeled by a probabilistic distance-dependent bond formation criterion: if a particle of type 1 (unreacted end group) is located within a specified distance of a particle of type 2 (active radical), a bond is formed between the two with a specified probability p_{bond}. The type 2 particle is changed to a type 4 particle (reacted end group), and the type 1 particle becomes a type 2 particle (active radical). The check for the polymerization reaction is only performed at specified intervals during the course of the simulation. This amounts to three parameters: the bond formation distance R_{cut}, the probability of bond formation p_{bond}, and the frequency of bond formation attempts N_r (expressed as the number of simulation steps between reaction attempts). Similarly, if two type 3 particles (active radicals) are within R_{cut} of each other, a bond is formed between them with probability p_{bond}, and both particles are set to type 4 (reacted end group). Both types of bonds that are formed are treated using the same harmonic form as intramolecular bonds discussed above; in the absence of atomistic simulations of the polymerized system, we simply set the parameters for the newly created bonds to be the same as those for the site 1-2 bonds (see figure 2.2).

The overall reaction rules are summarized below, with all associated parameters in bold text. The schematic in Figure 2.3 illustrates several examples of possible reactions.

- Initiation: at the start of the simulation, a fraction $\mathbf{x_i}$ of all active radicals are randomly selected to be switched to type 2 (active radicals) or type 3 particles (inactive radicals). The ratio of type 2 particles to the total of type 2 and type 3 particles is $\mathbf{K_a}$.

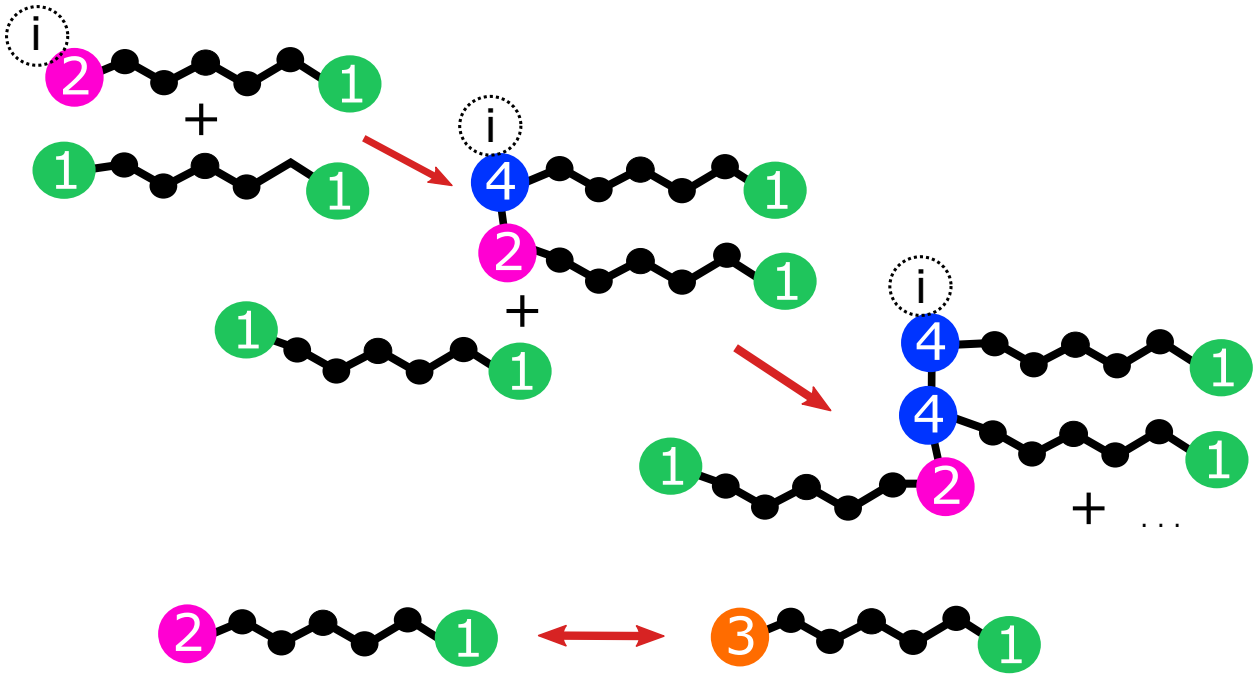

Figure 2.3. Examples of possible reactions in the simulations. Numbers indicate particle types. Lowercase 'i' indicates an initiator molecule, which is not explicitly included in the simulations. Top: polymerization/chain elongation. Bottom: activation/deactivation reaction

- Activation/deactivation: every $\mathbf{N_a}$ simulation time steps, each type 2 and type 3 particle is checked. Regardless of its current type, each particle is set to type 2 with a probability of K_a, or to type 3 with a probability of $1 - K_a$.

- Polymerization reaction (elongation): every $\mathbf{N_r}$ simulation time steps, distances between type 1 and type 2 particles are checked. If a pair is closer than a specified distance $\mathbf{R_{cut}}$, a bond is formed with probability $\mathbf{p_{bond}}$, and the particle types are changed from 1 to 2 and from 2 to 4.

- Termination reaction (annihilation): if two active radicals (type 2 particles) are within R_{cut} of each other, a bond is formed, and both particles are changed to type 4.

All aspects of the reaction model were implemented in the LAMMPS molecular dynamics code [43], as modifications to the "fix bond/create" code. The time step in simulations was $0.005\ \sqrt{(\epsilon/\sigma^2)}$, and simulations were carried out in the NPT ensemble (isothermal/isobaric) at a temperature of $0.8\ \epsilon$ and a pressure of $1.0\ \sigma^3/\epsilon$. A range of parameters associated with the ATRP model were tested, as discussed in section 3 below.

Atomistic simulations of the UDMA monomer

Urethane dimethacrylate (UDMA) molecules were built using the Enhanced Monte Carlo (EMC) code [27] version 9.3.8, with zero-temperature equilibrium bond lengths, angles and dihedrals defined by the OPLS potential [30, 31] (See OPLS parameters in Appendix B.3). Each monomer consisted of 71 atoms, 70 bonds, 124 angles and 158 dihedrals (See LAMMPS Data File in the Appendix B.4). Once built, classical molecular dynamics simulations were carried out using the LAMMPS code [43]. The UDMA monomer morphology was evolved in both isolated single molecule simulations, as well as bulk density simulations. The goal of these fully-atomistic simulations was to provide a set of training data from which a coarse-grained model could be parameterized. The single monomer simulations were used to constrain the number of beads per monomer, while the bulk simulations were used to set bond lengths and angles between sites, and corresponding strengths of each coarse-grained interaction.

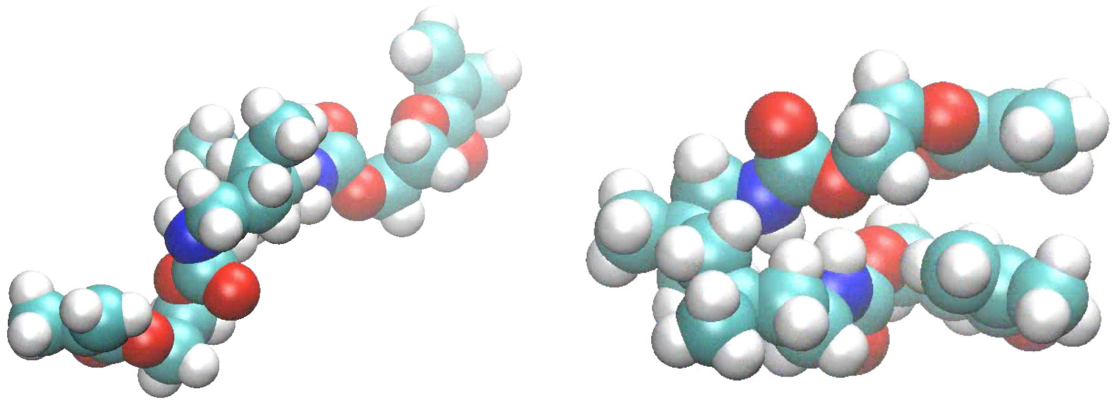

Figure 2.4. Molecular dynamics snapshots of single UDMA monomer molecules showing both extended (left) and folded, or compact (right) conformations. Single monomer simulations were carried out in vacuum, using a Langevin thermostat to model an implicit poor solvent at 300 K.

The single molecule simulations were carried out in vacuum, using a Langevin thermostat, to investigate the molecule's bending modes in an implicit poor solvent. A single molecule, with maximum extension of less than 1.0 nm, was modeled in a 5 nm cubic periodic cell to assure no self-interaction. Initial studies were conducted in two potentials, OPLS [30, 31] and ReaxFF [53, 8]. In both the bonded and reactive potentials, the single molecule was able to explore both extended and folded conformations. These qualitative observations pointed toward a coarse grained model with five or seven sites and a symmetric structure centered about a flexible middle site. Figure 2.4 shows examples of a single UDMA molecule in extended and folded arrangements. After initial tests with a five-site model, we selected the seven site model for the majority of CG simulations as it strikes a good balance between

capturing the conformational flexibility of the monomer and providing a computationally expedient model (see figure 2.6).

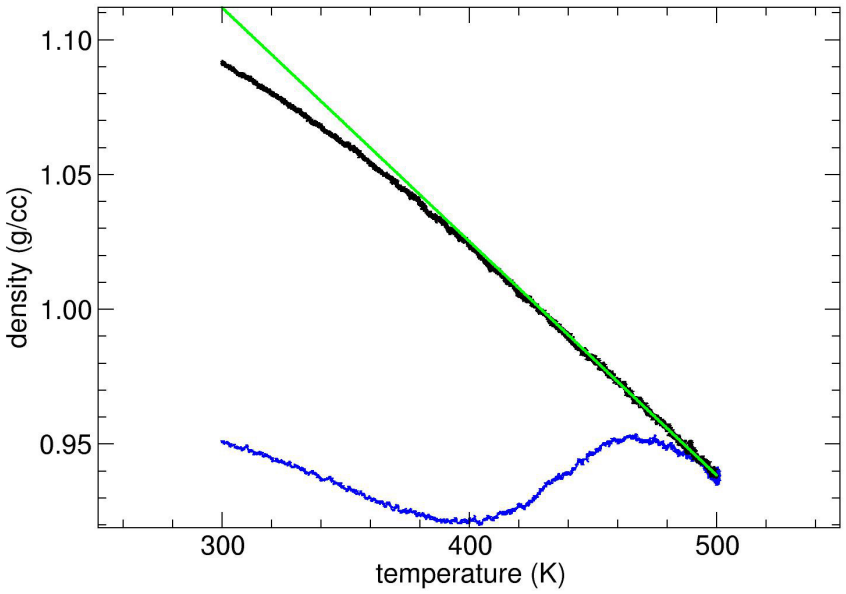

Figure 2.5. Density as a function of pressure during final anneal to 500 K (blue curve) followed by a quench down to 300 K (black curve). The quench follows a linear trend (green line) in density vs. temperature down to approximately 400 K. From this plot, one can deduce a T_g in the range of 375 to 400 K.

The bulk density UDMA monomer melt was constructed from 10 648 replicas of the monomer, compressed instantaneously to 14.1 nm $\times$ 14.1 nm $\times$ 18 nm, then equilibrated in an NPT ensemble at 300 K and 1 atm for 3 ns. The equilibrated melt had a density of 0.95 g/cc, before a final 1 ns anneal at 500 K. The annealed sample was then cooled at a quench rate of 50 K / ns to reach a final density of 1.091 g/cc at 300 K. Figure 2.5 shows a plot of the density vs temperature during the anneal and quench process. From the deviation of the quench curve (black) from the linear fit (green) we can deduce a glass transition temperature, T_g of between 375 and 400 K.

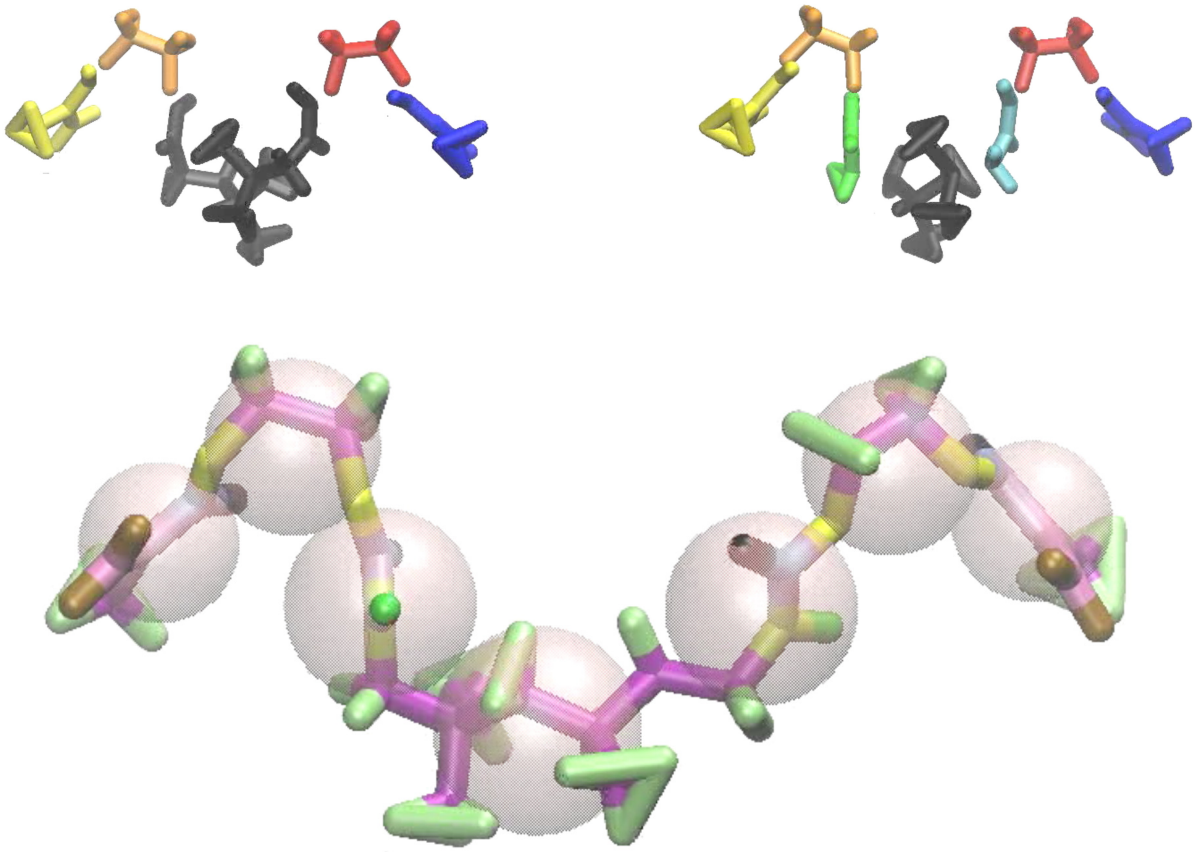

Figure 2.6. Depictions of the UDMA monomer divided into 5 beads (top left) and divided into 7 beads (top right). The atoms are colored to correspond to the bead. (bottom) The atomic positions are overlayed with spherical beads of approximately equal size to represent the CG7 model.

Chapter 3

Results and Discussion

Cure kinetics and cure analysis

Cure analysis of UDMA is visited in this section; data for BisGMA/TEGDMA can be found in the appendix. UDMA cure kinetics were assessed from mid-FTIR absorption data (Figure 3.1). The integrated area of the absorption at 1637 cm^{-1}, corresponding to the unsaturated bond of the methacrylate, was used to assess the state of cure in-situ (Figure 3.2). A cure state calibration was completed using ratios of UDMA to an inert polymer, giving a quadratic function of integrated area with respect to percent concentration of UDMA at 23 °C, 70 °C, and 90 °C (Figure 3.3).

Three time resolved polymerization reactions of UDMA were used for the kinetic analysis: two reactions using 1% AIBN as initiator at 70 °C and 90 °C (traditional cure), and a controlled cure using ARGET ATRP with a monomer to initiator ratio of 160:1. From these two data sets we are able to calculate the state of conversion with respect to time for the three reactions being analyzed (Figure 3.4).

Conversion time data were fitted to a modified form of the rate equation originally proposed by Kamal [33] as a semi empirical equation for etherification reactions using a "diffusion factor" on each rate constant.

$$\frac{d\alpha}{dt} = (k_1 + k_2\alpha^m)(a_f - \alpha^n) \tag{3.1}$$

$$k_i = \frac{k_{i0}}{1 + \exp\left(\pm C(\alpha - \alpha_c)\right)} \tag{3.2}$$

The differential equation 3.1 was solved using one of Matlab's built in ordinary differential equation solvers, and the constants were fitted minimizing the norm of the interpolated solution and the experimental data points using a simplex search algorithm, also in Matlab. Here, α is the relative degree of cure, and the remaining symbols are constants. This equation, though originally semi empirical, is modified as follows: instead of unity, a term a_f is introduced, which allows for a final conversion state of less than unity; and the diffusion factor is introduced, which effectively causes a transition regime where k_2 is dominant and

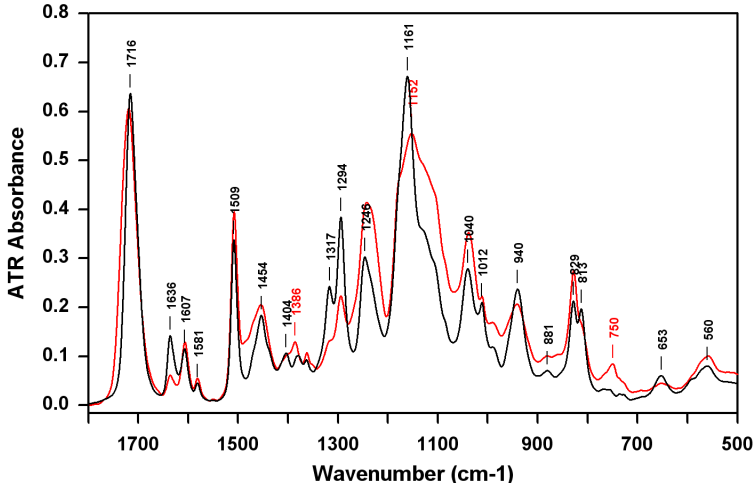

Figure 3.1. FTIR spectra of UDMA cured with 1 wt. % AIBN before (black) and after (red) cure at 70 °C. The peak at 1636 cm^{-1} is associated with the C=C of the methacrylate and is used to calculate extent of cure.

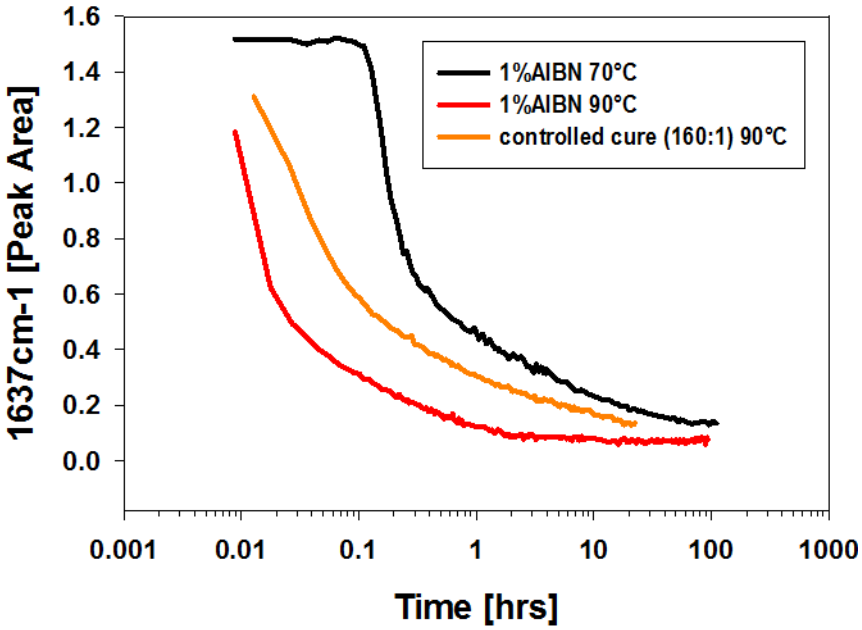

Figure 3.2. Area of 1637 cm^{-1} (C=C group of methacrylate) band as a function of time for UDMA cured with (black) 1 wt.% AIBN at 70 °C, (red) 1 wt.% AIBN at 90 °C, and (orange) ARGET ATRP (160:1 methacrylate:initiator) at 90 °C.

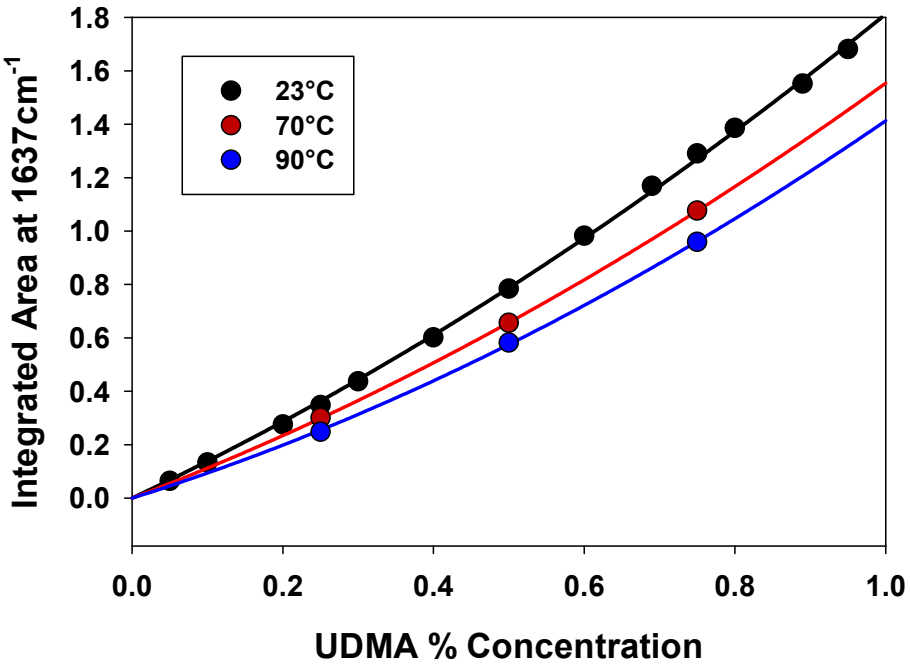

Figure 3.3. Calibration curves for UDMA at (black) 23, (red) 70, and (blue) 90 °C.

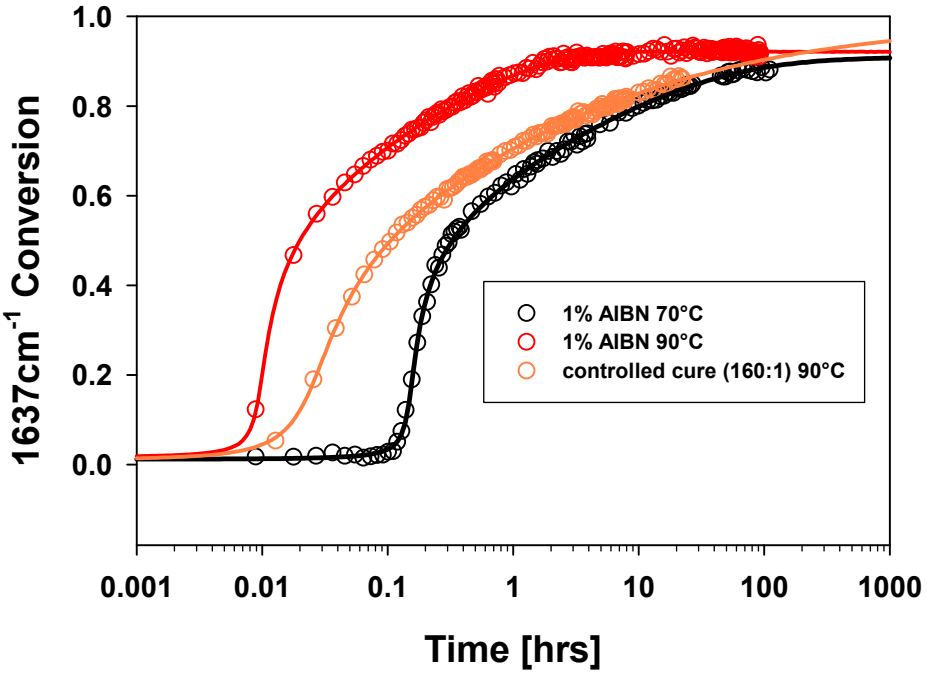

Figure 3.4. Conversion rate as a function of time for UDMA cured using TRP with 1 wt.% AIBN at (black) 70 and (red) 90 °C, and ARGET ATRP with monomer ratio 160:1 (orange) cured at 90 °C. Open circles represent experimental data and lines represent curve fits to that data as described in Equation 3.1.

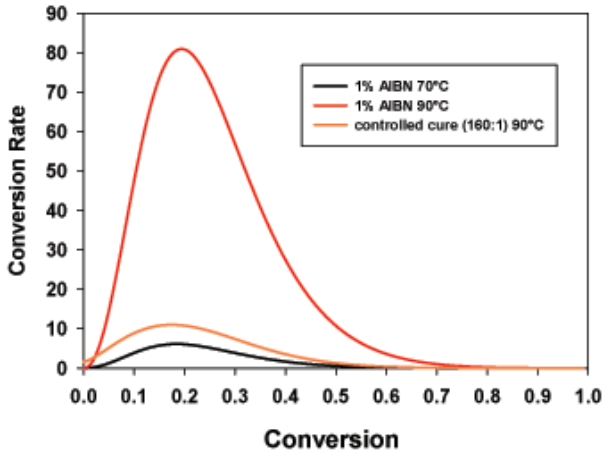

Figure 3.5. Conversion rate as a function of conversion for UDMA cured using TRP with 1 wt.% AIBN at (black) 70 and (red) 90 °C, and ARGET ATRP with monomer ratio 160:1 (orange) cured at 90 °C.

constant for all $\alpha < \alpha_C$ and decreases exponentially for all $\alpha > \alpha_C$ ($C > 0$), k_1 being inversely conversion dependent ($C < 0$). Thus, the equation appears to be wholly empirical as there are effectively seven constants along with a variable initial condition capable of modifying its shape and time placement. The fitted constants extracted from the fit therefore lack any theoretical backing for describing mechanistic kinetics.

However, the equation allows for an almost perfect fit of the data, seen as the solid lines in Figure 3.4, and will allow for an evaluation of particular aspects involved in the reaction. One particular feature is the shape of the conversion rate as a function of conversion as seen in Figure 3.5. This shape suggests a maximum conversion rate at 18%, 19% and 17% conversion for the 70 °C traditional, 90 °C traditional, and 90 °C controlled cure respectively. Another aspect is the suggestion of an activation energy between the 90 °C and 70 °C for the initial part of the reaction ($\alpha < 0.4$) of 143 kJ/mol, and a temperature variant diffusion regime for the latter part of the reaction ($0.6 < \alpha < 0.8$). Finally, the fit allows for a slight extrapolation which approaches the fitted variable a_f and suggests a final conversion state of 90%, 92%, and 99% for the traditional 70 °C and 90 °C, and 90 °C CRP respectively, although extended time runs for the 70 °C and controlled cure are necessary to verify these numbers.

NMR was employed as as secondary verification of extent of cure. 13C solution state NMR was used to assess the state of the pre-cured monomer (Figure 3.6) while solid state 13C MAS NMR analyzed the cured materials. The peaks of interest are the resonances a and c, which are expected to disappear during polymerization. Figure 3.7, shows an overlay between the solution 13C NMR and solid state 13C MAS NMR for the controlled cure material after 90 °C cure for 20 hours. The resonances at $\delta = 167$ and 136 ppm clearly show

that there are unreacted monomer vinyl groups still present in the material, while the new resonance at $\delta = 177$ ppm results from the new carbonyl O-CO-CH_2 in the polymer following vinyl reaction. The carbonyl at $\delta = 156$ ppm (b) does not shift with polymerization, as would be expected since it is interior to the reactive vinyl end.

Figure 3.8 shows an example of deconvoluted spectra for BPO and 160:1 ARGET ATRP samples cured at 90 °C for 20 hours in the carbonyl and vinyl region. While the controlled cure UDMA polymer sample still has unreacted vinyl species, these vinyl species are not as prominent in the BPO-cured sample. Furthermore, the chemical shift of the two carbonyl resonances (157 and 176 ppm) is similar between the two samples, suggesting that there is not a major change in the hydrogen bonding structure for these two materials. Estimations of the remaining vinyl concentrations were made on the samples by normalizing to the internal carbonyl signal ($\delta = 157$ ppm) . This is based on single pulse Bloch decay direct spectra estimates. Vinyl concentrations for the BPO-cures sample were $2.26/49.9 = 4.5\%$ and $15.3/50.87 = 29.4\%$ for the controlled cure material. Of note is that the two carbonyl resonance integrals were 1:1, which is expected for the BPO-cured sample (low vinyl concentration) while for the controlled cure the sum of the vinyl and new carbonyl add to an approximately 1:1 ratio. Finally, differences in the cross polarization efficiency were noted between the two polymer samples and point to significant differences in the local chain mobility. Detailed investigation of these dynamics was not conducted.

After comparing the extent of cure using NMR to mid-FTIR, it was clear that there were major discrepancies between the two. The position of the methacrylate band in mid-IR would likely benefit from deconvolution, although it's not clear at this point whether this would provide improve accuracy of the quantitative results for monitoring the extent of reaction as a function of time. Thus, this is a cautionary note to always verify IR extent of cure data with a secondary method. Since mid-IR was unable to be used with our current methodology to monitor cure kinetics or extent of cure, near-FTIR was evaluated instead. The 6165 cm^{-1} band was assigned to the methacrylate group and analysis of extent of cure was done using a calibration curve. Near-IR was found to have similar values (within 5%) of extent of cure as those determined using NMR. Therefore, extent of cure was re-assessed using this technique. Table 3 compares the extent of cure for the UDMA thermosets as a function of polymerization chenistry and cure temperature. After these data were compiled, it was determined that a post-cure above T_g was necessary for the CRP samples in order to reach similar extent of cure as the TRP samples. The same post-cure was applied to TRP samples to ensure similar thermal history for all materials.

DSC was used to verify the extent of cure results and also to determine cure kinetics. Heat flow versus time curves for TRP and CRP at all cure temperatures are shown in Figure 3.9. It is clear that there is very little residual cure present in the BPO systems as the temperature is raised to 150 °C for post-cure. In addition, the traditional cure occurs much more rapidly than the CRP cure. In both systems, the cure curve increases in area as the initial cure temperature is increased from 70 to 90 °C while the residual post-cure peak decreases. This clearly indicates that there is some unreacted species left in both systems and agrees with what was observed with NMR and NIR.

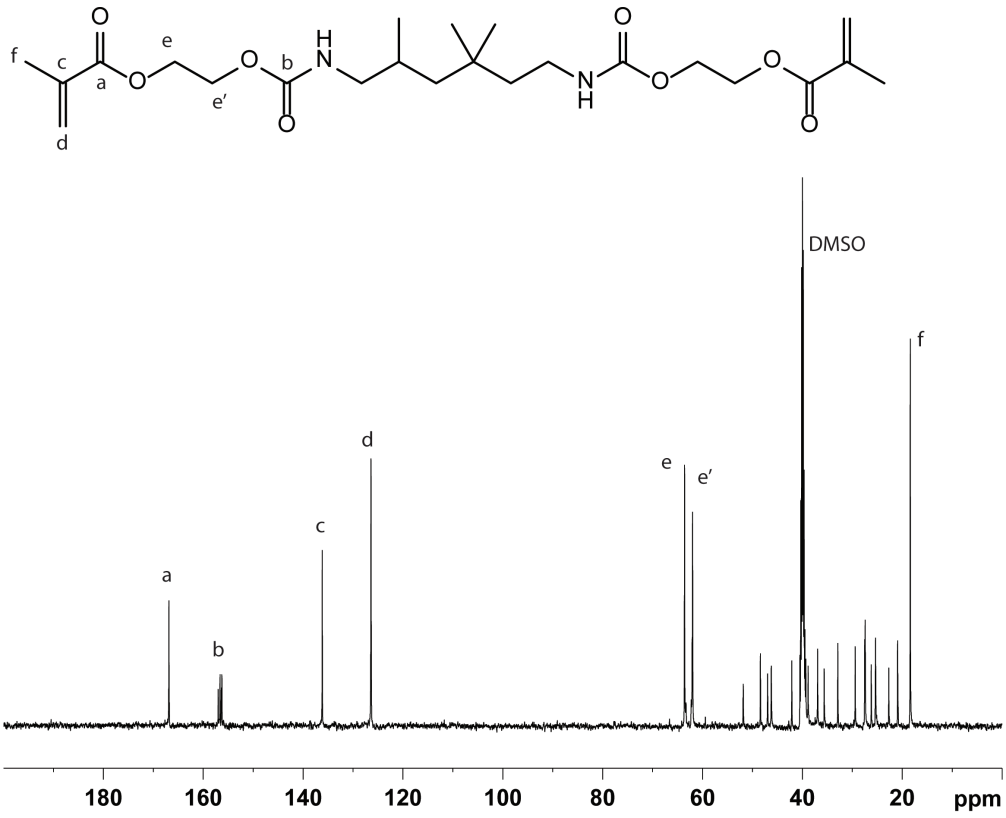

Figure 3.6. 13C solution state NMR of UDMA with labeled peaks.

Table 3.1. UDMA extent of cure as a function of polymerization mechanism and cure temperature. Post-cured samples were evaluated using NIR while values for those without post-cure were obtained with NMR.

	Extent of cure (%)			
	TRP		CRP	
Cure Temp. (°C)	no post-cure	post-cured	no post-cure	post-cured
70	94	95	52	94
80	96	97	63	95
90	99	99	73	95

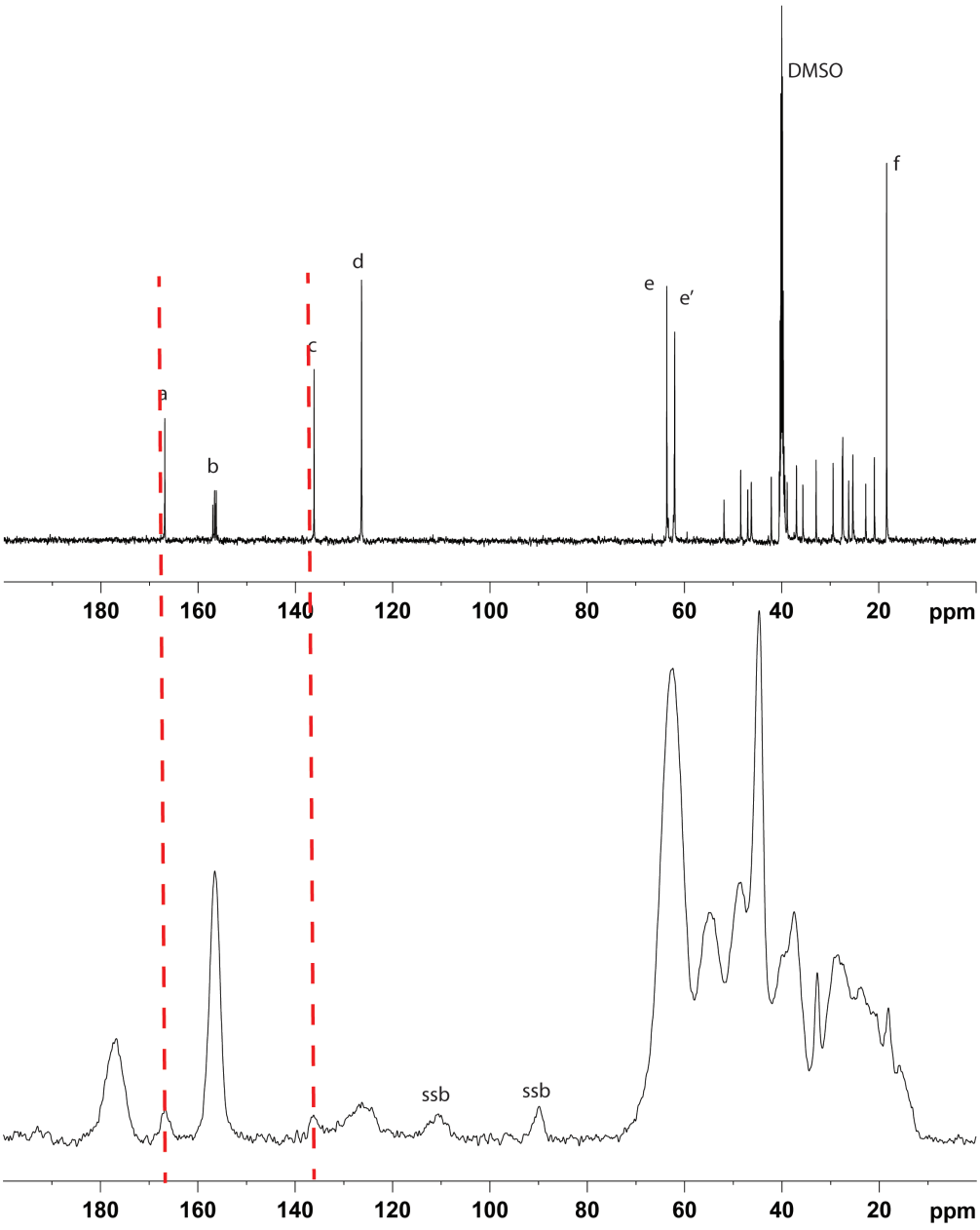

Figure 3.7. A comparison of the 13C solution state, uncured (top) and solid state, cured (bottom) NMR of UDMA. The solid state sample was cured at 90 °C using CRP with a monomer:initiator of 160:1.

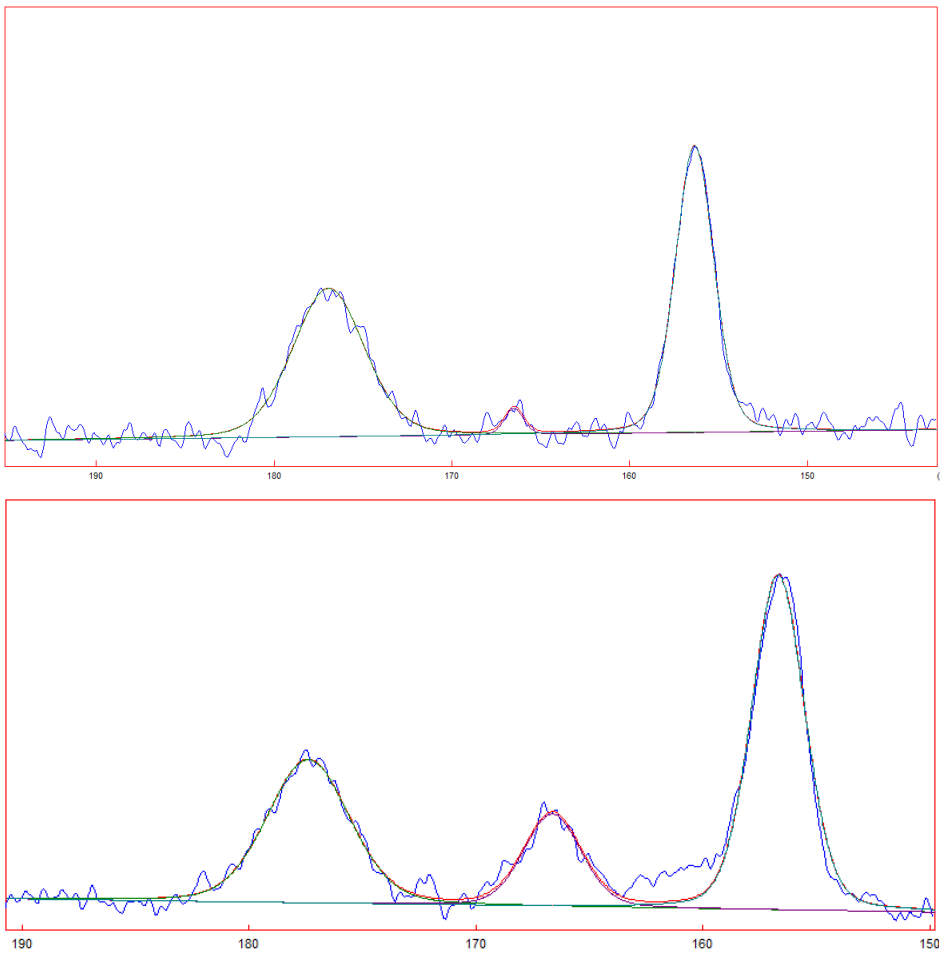

Figure 3.8. Quantitative deconvolutions of direct 13C MAS NMR spectra cured at 90 °C for 20 hours. Benzoyl peroxide cured (top) and controlled cure 160:1 (bottom).

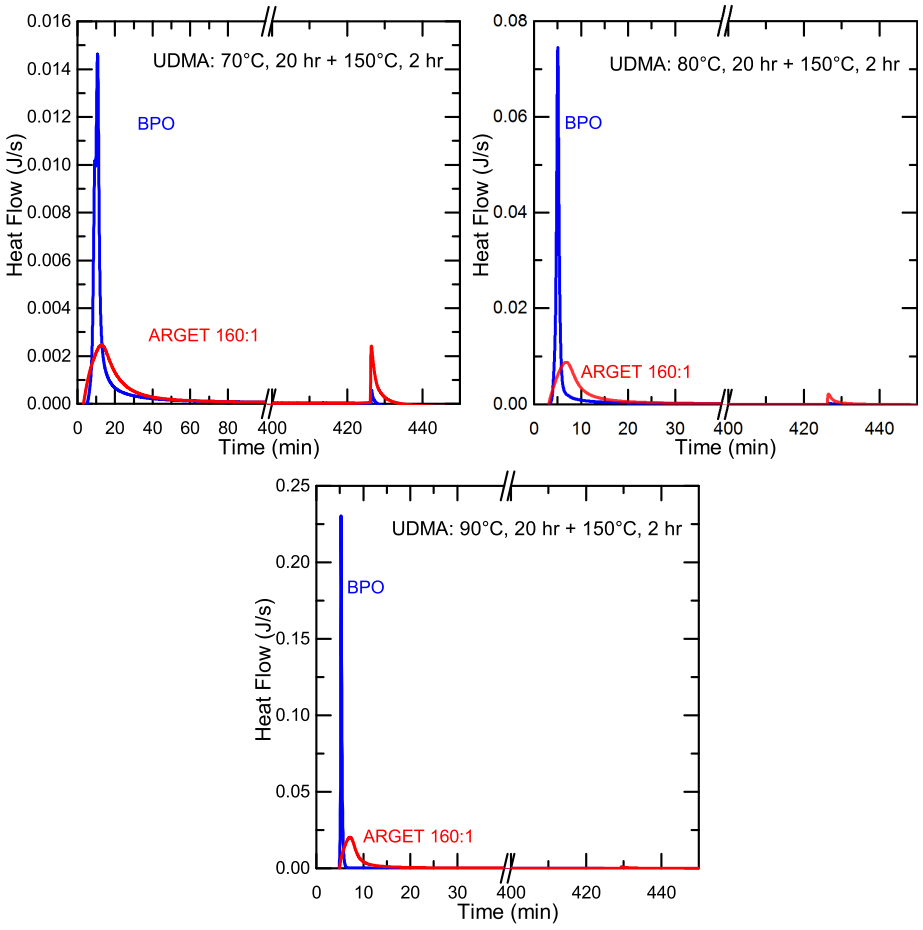

Figure 3.9. Heat flow versus time for all cure temperatures. Traditional cure using 1 wt.% BPO is shown in blue and ARGET ATRP 160:1 in red.

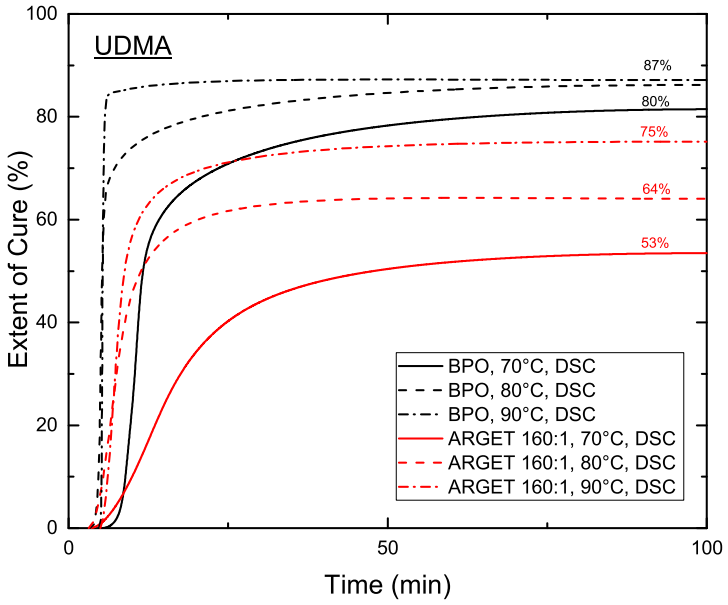

Figure 3.10. UDMA extent of cure versus time. Traditional cure using 1 wt.% BPO is shown in black and ARGET ATRP 160:1 in red. Solid, dashed, and dash-dot lines represent cure temperatures of 70, 80, and 90 °C, respectively.

Figure 3.10 shows the extent of cure versus time for TRP and CRP-cured UDMA as a function of cure temperature; these data were determined using DSC. Extent of cure is within 1% of NMR values for the ARGET ATRP-cured samples but off by 10 - 14% for the TRP cure. At this point it is unclear why the discrepancy between DSC and NMR exists for the TRP samples and requires further investigation. Nevertheless, these curves were used to generate rate of polymerization plots for both cure methods (Figure 3.11). TRP and CRP show an increase in polymerization rate and a decrease in the breadth of the cure peak as temperature is increased from 70 to 90 °C. However, polymerization rates differ by about an order of magnitude between the two, and while the TRP materials are all finished polymerizing within 10 minutes, CRP takes at least 10 - 40 minutes depending on temperature.

Mechanical Properties

Differences in the mechanical behavior of UDMA thermosets were uncovered between the two cure systems (Figure 3.12). Namely, UDMA cured with ARGET ATRP had lower values

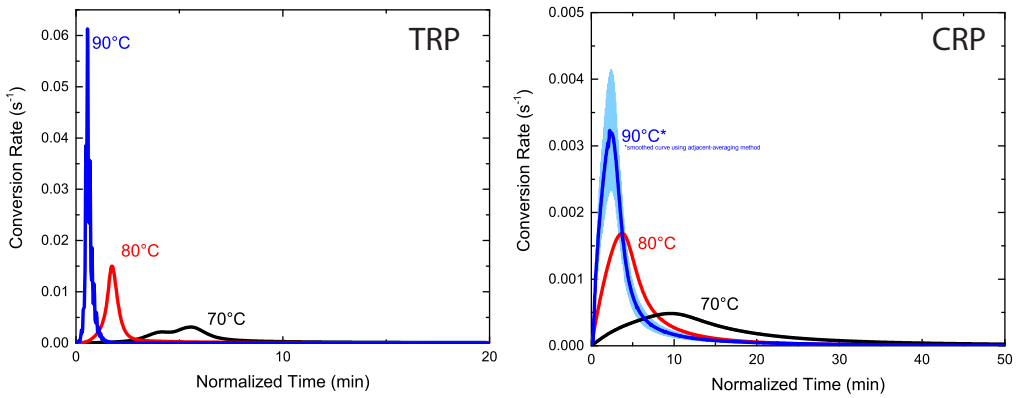

Figure 3.11. UDMA conversion rate versus time for TRP (left) and CRP (right). Black, red, and blue lines represent cure temperatures of 70, 80, and 90 °C, respectively. Time was normalized to the onset of curing.

of flexural modulus (slope of linear portion of stress strain curve) than those cured using a traditional radical polymerization, and did not fail during the test except in cases where surface defects that were not adequately polished out prior to testing (Figure 3.13) caused premature failure. The ATRP samples were capable of withstanding so much strain that tests had to be stopped as the material began slipping from the test fixture (Figure 3.14a). In addition, the CRP samples were able to recover from the induced stress after approximately four to eight minutes from being removed from the Instron (Figures 3.14 b & c). Furthermore, the flexural modulus of controlled polymerization samples showed a much stronger dependence on cure temperature where higher cure temperatures lead to higher values of flexural modulus than did TRP samples. However, these differences in mechanical behavior were attributed to the different extents of cure in CRP versus TRP systems as well as increasing extent of cure with cure temperature for CRP.

In order to address the different cure states of CRP samples and between CRP and TRP, materials were post-cured above T_g for two hours to reach near complete reactions ($\geq$94%). After post-cure, extent of cure was within a few percent for all samples. Figure 3.12 shows the stress/strain behavior of UDMA at the three different cure temperatures without post-cure (post-cure curves overlapped with the non-post-cured materials and were not shown for clarity) while Table 3 summarizes the average modulus, stress at break, and strain at break from those curves. Corresponding data for BisGMA/TEGDMA blends can be found in Figure 3.15 and Table 3.

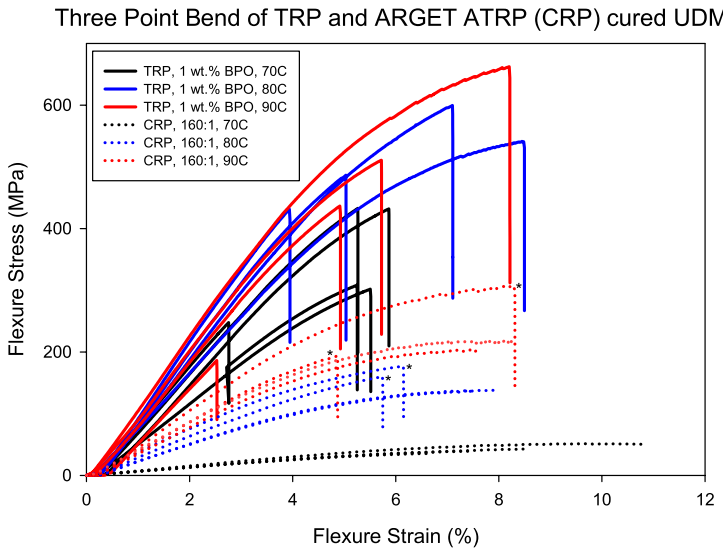

Figure 3.12. Comparison of stress vs. strain curves of UDMA cured with traditional and controlled polymerizations. Traditional polymerizations (solid lines) were carried out using 1 wt.% benzoyl peroxide and controlled polymerizations were carried out using ARGET ATRP (dotted lines) with a 160:1 ratio of monomer to initiator. Three samples were tested at each cure temperature of 70 (black), 80 (blue), and 90 °C (red). Asterisks indicate samples that failed prematurely due to surface flaws.

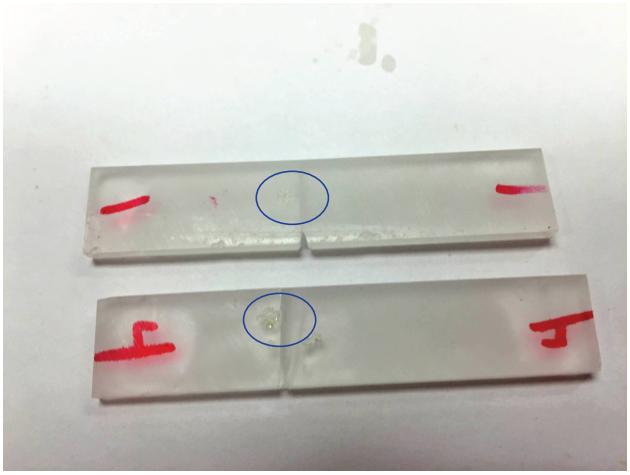

Figure 3.13. Photos of UDMA three-point bend specimens after failure with defects circled. We believe these surface defects are responsible for premature failure.

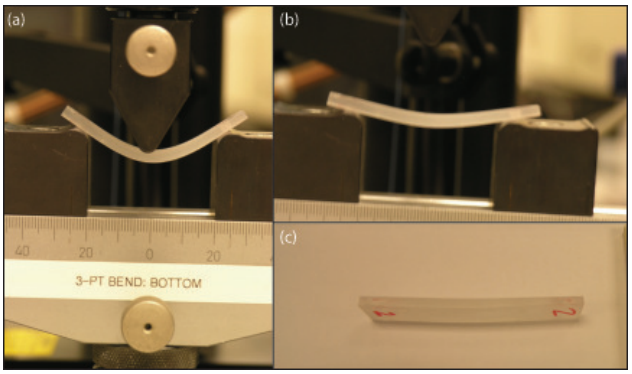

Figure 3.14. Photos of UDMA (a) during, (b) immediately after, and (c) eight minutes following three point bend testing.

Table 3.2. UDMA flexural modulus, stress at break, and strain at break as a function of cure temperature and cure method. All of the data is for post-cured materials.

	TRP			CRP		
Cure Temp. (°C)	E_f (GPa)	σ_b (MPa)	ε_b (%)	E_f (GPa)	σ_b (MPa)	ε_b (%)
70	2.5 ± 0.47	98.0 ± 19.5	5.5 ± 0.3	3.1 ± 0.17	93.7 ± 45.0	4.2 ± 2.2
80	2.7 ± 0.45	84.1 ± 26.9	4.5 ± 1.4	2.8 ± 0.09	109 ± 20.8	4.5 ± 1.5
90	2.9 ± 0.18	118 ± 20.3	4.6 ± 1.9	2.9 ± 0.23	97.3 ± 26.3	3.8 ± 1.4

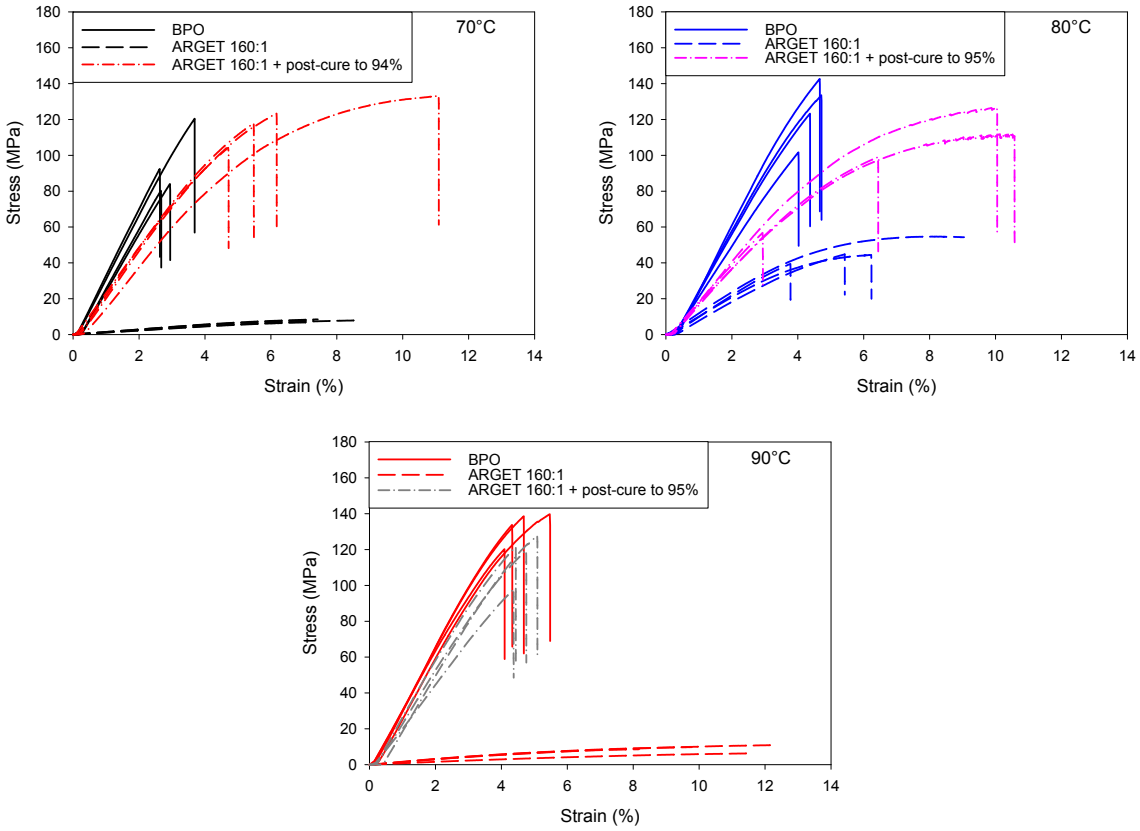

Figure 3.15. Stress versus strain curves of Bis-GMA/TEGDMA 70/30 cured using TRP (straight lines) and CRP (dashed lines) obtained from three point bend. Initial cure temperatures are listed in the top right corner of each figure. Also plotted are the ARGET ATRP 160:1 samples with post-cure to c.a. 95% (dash-dot lines) to allow for a direct comparison of TRP and CRP at similar EC.

Table 3.3. BisGMA/TEGDMA flexural modulus, stress at break, and strain at break as a function of cure temperature and cure method. All of the data is for post-cured materials.

	TRP			CRP		
Cure Temp. (°C)	E_f (GPa)	σ_b (MPa)	ε_b (%)	E_f (GPa)	σ_b (MPa)	ε_b (%)
70	3.4 ± 0.23	94.3 ± 18.2	3.0 ± 0.5	2.4 ± 0.24	115 ± 8.10	6.9 ± 2.9
80	3.3 ± 0.36	104 ± 27.5	3.9 ± 0.7	2.1 ± 0.12	112 ± 13.9	7.5 ± 3.5
90	3.5 ± 0.12	129 ± 44.6	4.0 ± 1.1	2.8 ± 0.32	117 ± 13.0	4.7 ± 0.3

Network analysis

While our literature investigation suggested that using controlled radical polymerization could lead to the formation of improved homogeneity in chain polymerized thermosets, the extent to which this occurs has yet to be quantified. Several techniques including DSC, NMR, AFM, XRD, and SAXS were used to address this issue.

The glass transition temperature of UDMA cured with 1 wt. % benzoyl peroxide and 160:1 monomer to initiator ARGET ATRP at 90 °C was investigated using differential scanning calorimetry. Figure 3.16(a) shows the DSC trace for the traditional cure and Figure 3.16(b) for the controlled cure materials. The glass transition temperature appears to be around 126-127 °C for both cure systems. It is of note that these systems were not fully cured during the initial temperature ramp, so this value of T_g would be representative of the material following a post-cure procedure. The BisGMA/TEGDMA blend had a slightly higher T_g of approximately 154 °C when cured with BPO (see Appendix A).

1H NMR was used to analyze the sol fraction remaining in the cured thermosets to determine if the residual vinyl was associated with the original monomer or perhaps a partially reacted species (e.g. dimer, trimer, etc.). In the original monomer the vinyl protons are at 6.0 and 5.7 ppm, each having an integral of one (Figure 3.17(a)). The species of interest are the methylene protons OCH_2CH_2O near 4.2 ppm which had an integral of four. Sol was extracted using DMSO and the vinyl resonances were clearly visible from that sample (Figure 3.17(b)), again demonstrating the presence of unreacted species. In addition the ratio of the vinyl to the methylene protons in the sol remained four, arguing that the species obtained in the extraction was unreacted monomer, and not some small dimer, trimer, etc. However, partially reacted monomer still attached to the main polymer backbone (i.e. pendant double bond) would not be extracted and not assessed as part of the sol.

Solvent extraction was employed to determine the swelling factor and gel content of the materials. The data for BisGMA/TEGDMA is presented in Table 3. The uptake factor for the post-cured BisGMA/TEGDMA did not change based on initial cure temperature or cure method. Furthermore, while gel content stayed the same in the TRP system as a function of cure temperature, it increased in CRP with increasing cure temperature. This data is in general agreement with the extent of cure data presented previously.

AFM analysis (Figure 3.18) was conducted on the BisGMA/TEGDMA system for samples cured at 90 °C, with major problems associated with charging on the surface of the samples. It is difficult to draw quantitative comparisons between the TRP and CRP systems at this time, especially since it was established that the CRP sample required post-cure to reach similar extent of cure as the TRP sample. While we were unable to further explore this area, we believe that AFM should be looked at in the future as a quantitative way to measure network heterogeneity. This could be accomplished using image analysis software to analyze the area of hard to soft segments in the samples and comparing the ratios of TRP versus CRP.

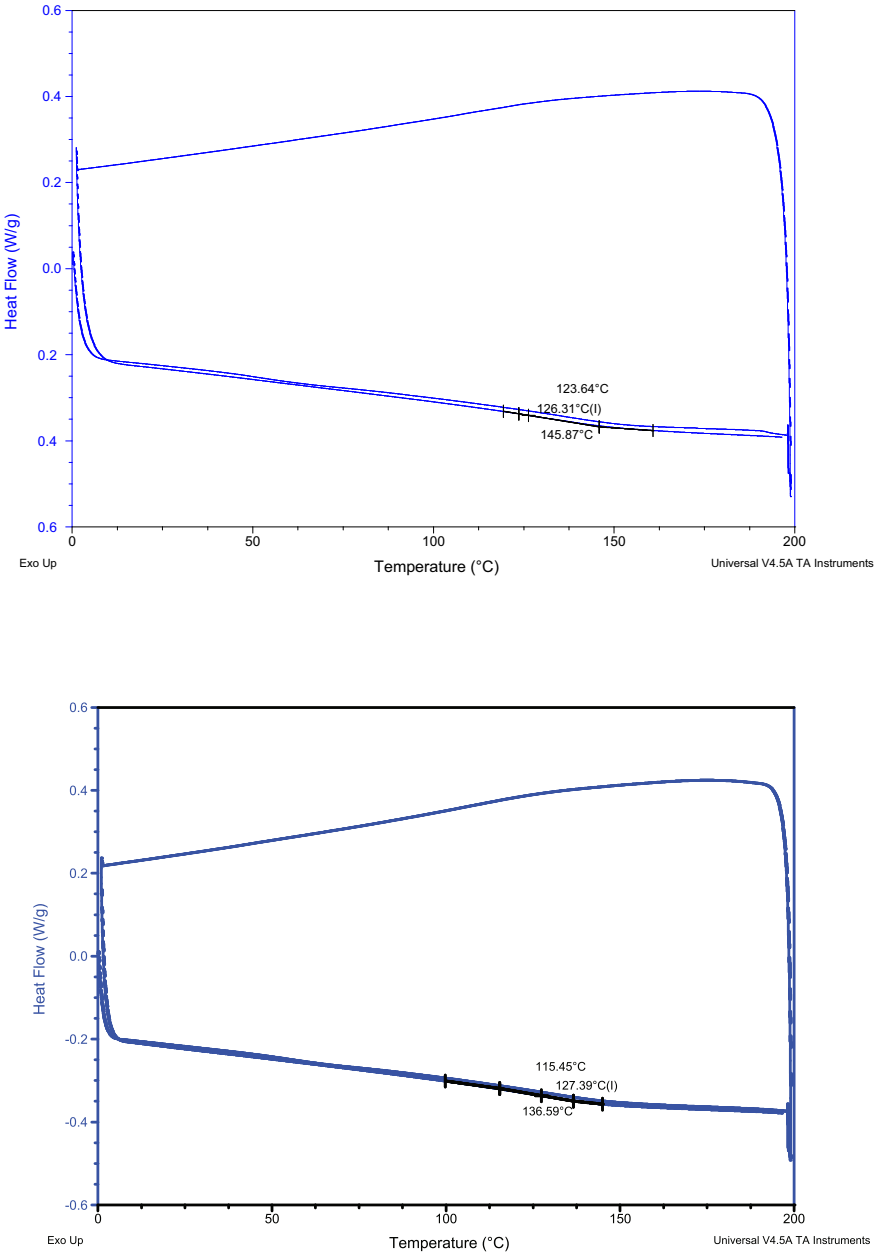

Figure 3.16. DSC trace of UDMA cured with benzoyl peroxide at 90 °C (top) and with ARGET ATRP having a monomer to initiator ratio of 160:1 (bottom). The glass transition temperature appears to be around 126 °C for the TRP cure and 127 °C for the CRP cure.

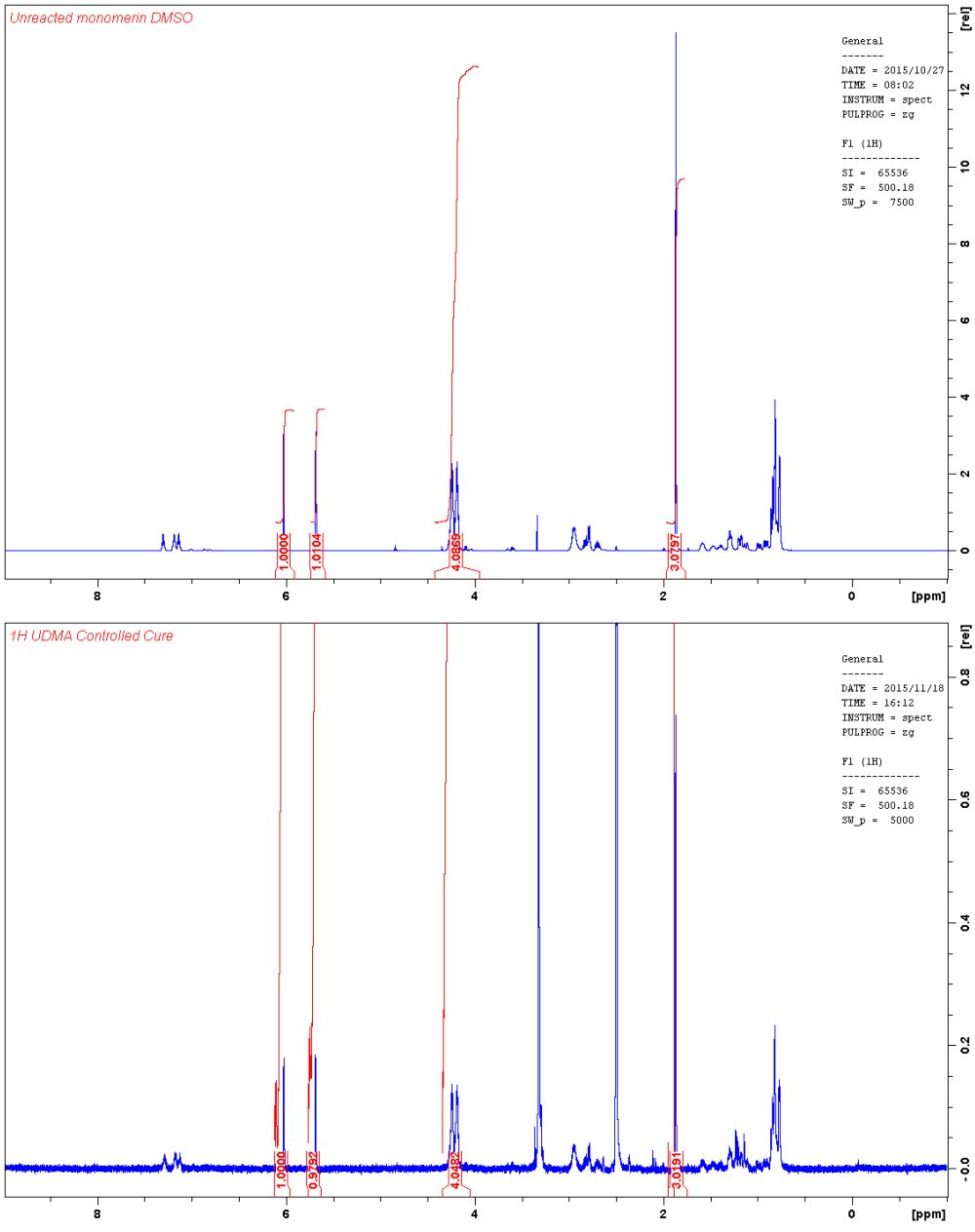

Figure 3.17. 1H NMR spectra of unreacted UDMA monomer (top), and DMSO-extracted sol (bottom) from a 160:1 ARGET ATRP sample cured at 90 °C for 20 hours.

Table 3.4. BisGMA/TEGDMA gel content and solvent uptake as a function of cure temperature and cure method. All of the data is for post-cured materials and is the average of three samples.

	TRP		CRP	
Cure Temp. (°C)	Uptake Factor	Gel Content (%)	Uptake Factor	Gel Content (%)
70	1.0	99.1	1.4	94.1
80	1.0	99.1	1.3	95.8
90	1.0	99.2	1.4	98.2

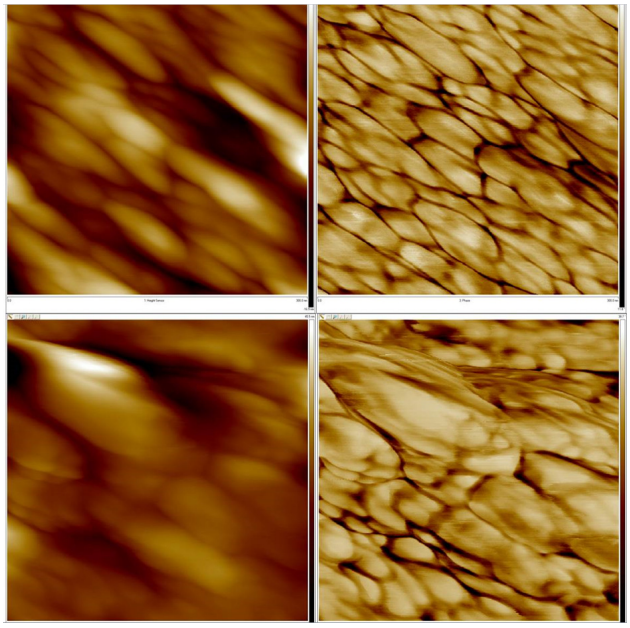

Figure 3.18. AFM height images (left) and phase (right) of AIBN-cured BisGMA/TEGDMA blend at 90 °C (top) and ARGET ATRP-cured BisGMA/TEGDMA blend at 90 °C (bottom). Images are 300 × 300 nm and were taken in tapping mode.

X-ray scattering was employed as a secondary technique to uncover network morphology. The TRP system employed in this analysis used AIBN as the initiator and both TRP and CRP thermosets were cured at 90 °C. The combination of wide and small angle scattering techniques allows one to uncover a larger range of sizes which may be associated with the network. Scattering data from XRD is presented in Figure 3.19. The patterns for TRP and CRP look very similar in general appearance, with a broad peak centered around 2θ = 18 ° and a second peak near 2θ = 42 °. The first peak at 2θ = 18, in conjunction with Equation 2.3, was used to determine microgel size of the networks. Both of the cured TRP and CRP systems had microgel sizes of 10 ±1 Å. This is smaller than the 20 Å reported by Barszczewska-Rybarek in a 60/40 blend of BisGMA/TEGDMA cured using camphorquinone as an initiator and ultraviolet radiation to induce the crosslinking reaction [3].

Small angle x-ray scattering was only performed on the AIBN-cured sample (90 °C) before the detector went down and had to be repaired. As of the time of writing, the detector repair had not been completed. The scattering pattern observed in this system (Figure 3.20) had an initial slope of -3.9, which is close to -4, the expected value for a two-phase system with a sharp interface [9, 44]. The two-phase system is likely the result of the interface from two different monomers, BisGMA and TEGDMA, present in the system. The small bump at high q was due to an issue with background subtraction of the tape used to hold the sample in the instrument.

Clearly, it was challenging to find a way to quantitatively compare network heterogeneity between TRP and CRP cured systems and we were unsuccessful in our experimental efforts. Interestingly, stress/strain curves of the two different systems showed different behavior. Namely, the BisGMA/TEGDMA blend had improved strain at break with little sacrifice to modulus when comparing CRP to TRP, whereas the UDMA system showed no noticeable change between TRP and CRP systems. In step-polymerized epoxies, there is evidence to suggest that disparities in toughness enhancement using similar additives at similar extents of cure may be due to crosslink density, chain flexibility, and/or a combination of the two [41, 1, 10]. Extent of cure on our two methacrylate systems (UDMA and BisGMA/TEGDMA 70/30 w/w) were not identical, with the BisGMA/TEGDMA blend having a lower EC. In addition, chain flexibility of UDMA and BisGMA/TEGDMA is also dissimilar as evidenced by disparities between the two in T_g and flexural modulus. These factors will affect overall network ductility and may explain why the BisGMA/TEGDMA thermosets showed improved toughness whereas the UDMA did not.

Molecular dynamics simulations

.

Preliminary simulation studies used a simple five-site model of the UDMA monomer with all parameters set based on numerical convenience for purposes of testing and demonstrating the qualitative features of the reaction model. Atomistic molecular dynamics of the monomer

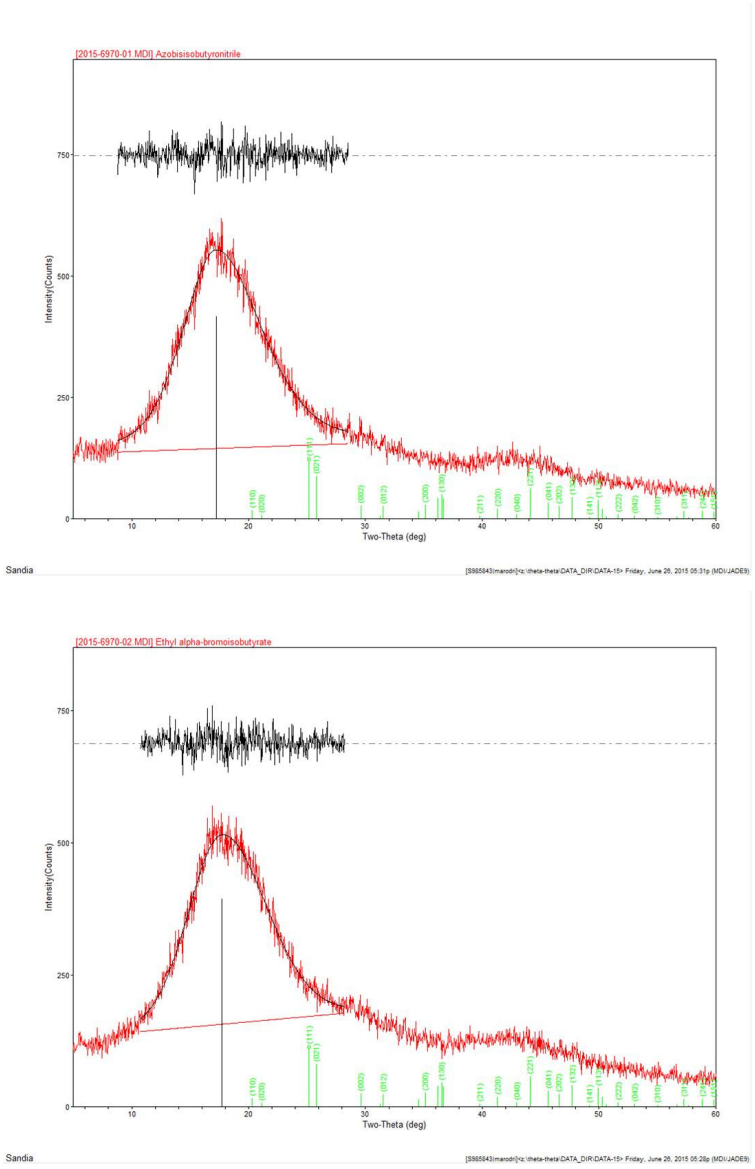

Figure 3.19. Wide angle X-ray diffraction patterns of (top) TRP cured with AIBN at 90 °C and (bottom) ARGET ATRP cured at 90 °C.

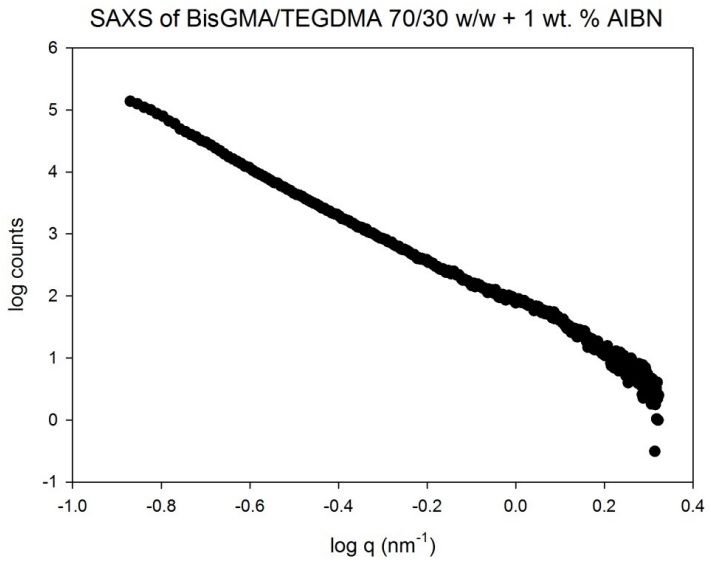

Figure 3.20. Small angle x-ray scattering data for Bis-GMA/TEGDMA 70/30 w/w blend cured with AIBN at 90 °C for 20 hrs.

melt suggested the importance of capturing the flexbility characteristics of the monomer and led to the use of an improved seven-site model, discussed in section 2. We present only the results of this more sophisticated seven-site model here; the preliminary results using the five-site model are summarized in the appendix.

The mapping between the atomistic and coarse-grained (CG) simulations discussed in section 2 focuses on the intramolecular degrees of freedom of the monomer and is used primarily to obtain a reasonable estimate of monomer flexibility characteristics. It does not address several other key parameters in the CG models, such as the simulation temperature. In principle the CG temperature could be mapped to the temperature used in experiments (and atomistic simulations) using e.g. the intramolecular bond energies; however, given the approximate treatment of non-bonded interactions and many other uncertain approximations involved in the CG model, we choose an alternate route. In experiments, the monomer melt is initially well above its glass transition temperature T_g, and as the reaction proceeds, the temperature increases and the mixture hardens. We do not attempt to replicate this fairly complex temperature and viscosity history, but instead keep the CG temperature constant to a value above the T_g of the monomer liquid. Figure 3.21 shows a plot of the monomer liquid simulation box volume as a function of the reduced temperature. While the determination of T_g is known to be sensitive to cooling rates and system size, here we are only interested in an approximate value. The change in slope in the plot corresponds to this value, which we take to be $T_g \approx 0.55$. We therefore use a temperature of $T = 0.8$ for subsequent polymerization simulations, which is well above the T_g of the monomer, as is the case in experiments.

The majority of simulations were carried out using a total of $\approx 20,000$ monomers. Due to

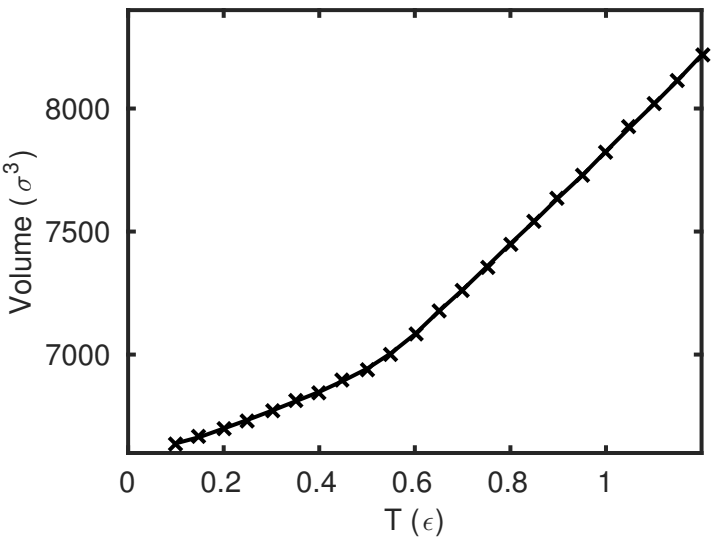

Figure 3.21. System volume as a function of temperature. The glass transition temperature T_g corresponds to the temperature where the slope changes.

the presence of two active sites on each monomer, the polymerization reaction in simulations results in the relatively rapid formation of a single percolating highly cross-linked polymer chain in all cases. Figure 3.22 shows a visual representation of this rapid chain growth based on snapshots at various extents of reaction for a typical CRP simulation. At relatively low reaction extents, there are several chains present (shown by distinct coloring); given the high availability of reactive sites, these chains grow quickly and continue to do so until they join to form a single percolating chain (blue coloring in figure 3.22). Remaining monomers and short oligomers are subsequently added as the reaction proceeds toward completion. Since the model only includes termination via the reaction of two active radicals (i.e. active radical annihilation), and active radical concentrations are relatively low, the absence of multiple chains is therefore not surprising. It is not clear that this is a feature also seen in experiments, but could in principle be confirmed by the distribution of molecular weight at various extents of reaction. However, we expect that simulations that reproduce the experimental molecular weight distributions are not feasible at this time, as they would require a prohibitively large number of monomers. Nevertheless, we believe the simulations capture sufficiently large length scales for the analysis of crosslink network topology.

Another feature noted in all simulations is a systematic decrease in volume (i.e. increase in density) as the polymerization proceeds, which is consistent with experimental observations. Figure 3.23 shows plots of the system volume as a function of simulation time and extent of cure. Typical volume shrinkage on the order of 5% for the seven-site model is typical regardless of polymerization parameters.

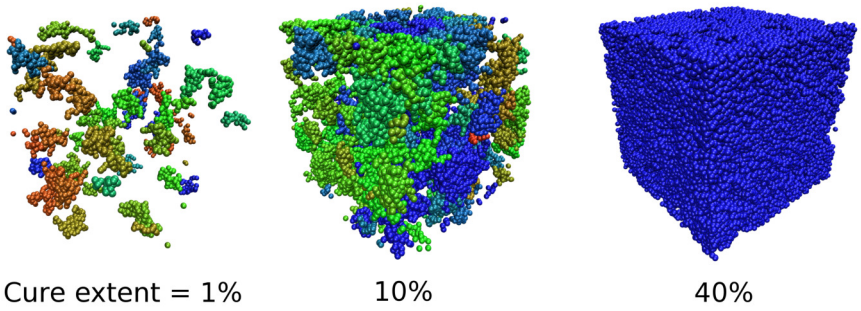

Figure 3.22. Visual representation of chain growth dynamics during polymerization for a typical CRP reaction ($x_i = 0.00625, K_a = 0.02, N_r = N_a = 1000$). Each distinct polymer chain is assigned a different color at various snapshots during the reaction. The formation of a single percolating polymer chain is observed at relatively low reaction extent values. For clarity, unreacted monomers are not shown.

We have carried out simulations for various values of the key polymerization parameters x_i, K_a, N_r and N_a (see section 2). The parameter x_i, which relates to the initator:monomer ratio (see section 2), is known from the experiments (1:160 = 0.00625 for CRP). In most simulations, we used the same value of x_i for both CRP and TRP to facilitate a more direct comparison; the value used in experiments for TRP is closer to 0.02, which we also tested in the simulations and found no significant differences from $x_i = 0.00625$ (data not shown). The remaining parameters can in principle also be measured and controlled experimentally, but no such data were available for the systems here. We therefore use a range of values that explore the relevant features of these systems. In particular, recall that as $K_a \to 1$, we recover a traditional radical polymerization (TRP) scheme, since the activation/deactivation reaction no longer takes place; as $K_a \to 0$, the reaction increasingly tends toward a controlled radical polymerization (CRP). Figure 3 shows the overall reaction kinetics as measured by the extent of cure vs. time for various values of K_a.

The reaction kinetics in the simulation are qualitatively similar to those observed in experiments (see figure 3.10), but there are several notable differences. First, there is a small initial increase in the rate of reaction in the experimental data that is absent in the simulations; this is likely due to the kinetics associated with the initiation reactions, which are treated as instantaneous in the simulations, resulting in the reaction rate (the slope of the curves in figure 3) being highest at the start of the simulations. As initiation is a relatively fast process, we do not expect this to a significant concern. In both experiments and simulations, as the reaction proceeds and monomer is depleted, the reaction rate decreases, and eventually plateaus as the final conversion is reached. However, in simulations, this always approaches complete (100%) conversion, whereas the experimental data show lower final conversions. We attribute this to a number of factors that allow monomers in the

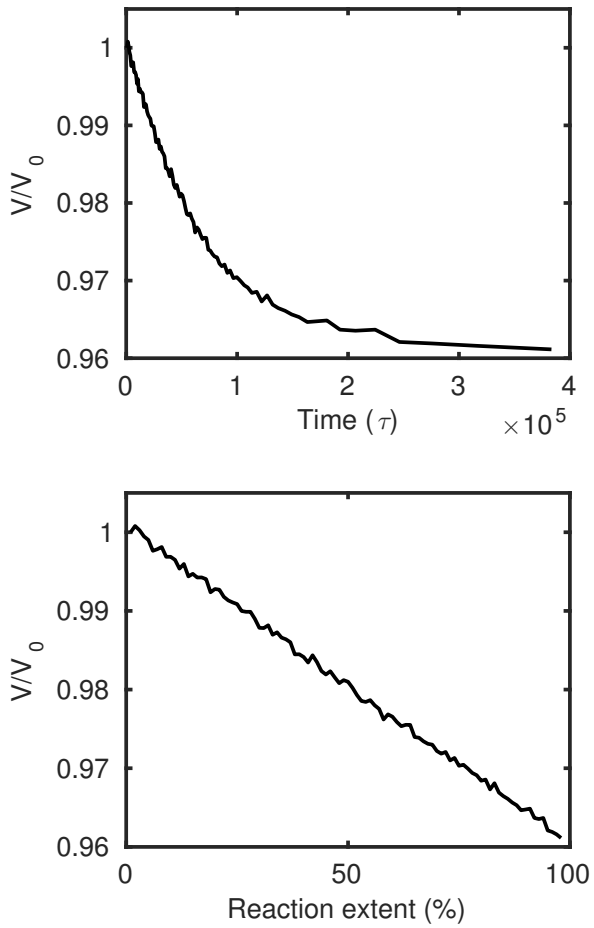

Figure 3.23. Volume shrinkage during cure in CG simulations. Data correspond to $x_i = 0.00625, K_a = 0.02, N_r = N_a = 1000$, but similar trends are observed regardless of polymerization scheme.

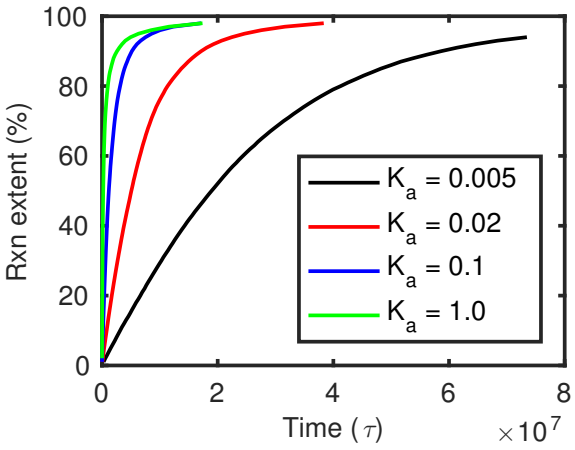

Figure 3.24. Overall reaction kinetics as a function of K_a, the fraction of radicals that are active. For the data shown here, $x_i = 0.00625$, $N_r = 1,000$, $N_a = 1,000$.

simulations to always diffuse to the many available free radicals: the fast dynamics due to the coarse-grained nature of the molecules, the relatively infrequent termination reactions, and the high availability of free radicals due to the di-methacrylate chemistry. In experiments, entanglement, additional mechanisms for termination and slow monomer diffusion could all effectively stop the reaction prior to completion; however, upon post-curing, relatively high conversions ($> 90\%$) are also observed experimentally.

Figure 3 shows the effects of N_r, the number of steps between reaction attempts. Not surprisingly, the reaction rate strongly depends on this parameter, with low values of N_r resembling kinetics of high K_a value reactions. The simulation time and hence computational effort required to achieve a given conversion is directly proportional to N_r. Even at the highest N_r values, the time scales of the reaction are still much faster than monomer diffusion time scales, which may be a significant shortcoming of the model, as this is likely not the case in experiments. We address this point in more detail below.

In addition to figures 3 and 3, we also tested the effects of the number of steps between reaction attempts N_a; the simulation temperature T; and the number of monomers, N. The reaction kinetics were only weakly sensitive to these parameters, as shown in the plots in the appendix; the exception to this is the temperature T, where a value of $T = 0.6$ near the monomer T_g (see figure 3.21) showed a considerable slowing of the reaction. Above T_g, the effect of the temperature was relatively minor. This is because the reaction in simulations is controlled by kinetics rather than diffusion, and there is no mechanism in the current model to adjust kinetic parameters (e.g. probability of binding or N_r) based on the temperature. Such a scheme can certainly be added, but the precise nature of it is unknown and would require detailed knowledge of the actual fundamental kinetic mechanisms.

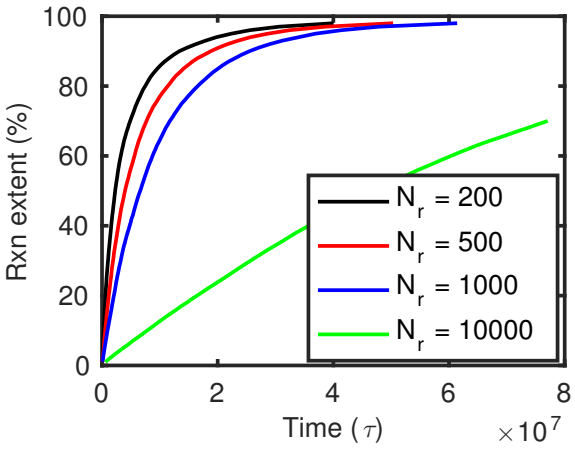

Figure 3.25. Overall reaction kinetics as a function of N_r, the number of simulation time steps between reaction events.

Network analysis

In this section we analyze the cross-linked polymer network topology based on the structures produced in CG simulations. Since all systems tend towards nearly complete conversion, a simple measure of the spatial distribution and heterogeneity of bonded and unbonded domains is not relevant. Instead, we attempt to quantify heterogeneity in the topology of the bonded network. Following Gavrilov et al who studied epoxy networks using MD simulations[18], we reduce cross-linked polymer structures to network graph representations [5]. In our approach, an active (methacrylate) site becomes a vertex of the graph, and a bond to another active site becomes an edge of the graph that connects two such vertices (this holds regardless of the state of the active site, i.e. active radical, free monomer, dormant radical, fully bonded). Additionally, two active sites (vertices) that belong to the same monomer are always connected by an edge. An example is shown in figure 3 below.

To quantify network topology, we have extracted several measures from the graph representations. In particular, for a given site (vertex), we compute what is known as the minimum closed cycle, defined as the minimum path required to return to that vertex without traversing any edge more than once. For example, in figure 3, for vertex 1, a minimum closed cycle is 1-4-5-2-1; for vertex 3, a minimum closed cycle is 3-2-5-8-3; vertices 6 and 7 have no minimum closed cycles. We have implemented a breadth-first search algorithm to efficiently compute all minimum closed cycles for a given structure, which we then histogram to construct a quantitative measure of network topology. Network homogeneity would correspond to a sharply peaked histogram, whereas network heterogeneity would show a broader distribution of minimum closed cycles.

Figure 3.27 shows the progression of the minimum closed cycle (MCC) histogram for several values of the parameter K_a at several reaction conversions. In all cases, histogram

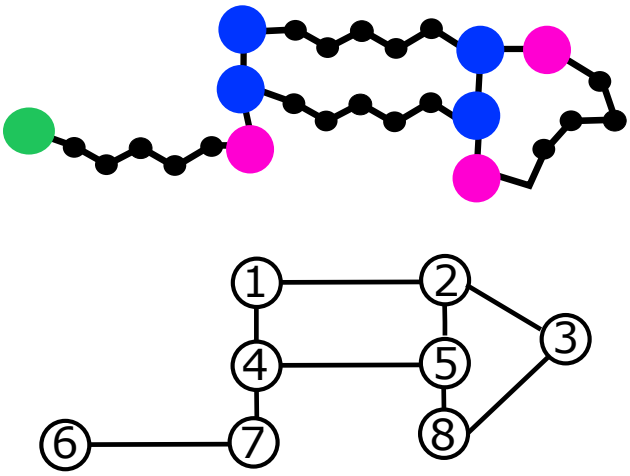

Figure 3.26. Network graph representation of a cross-linked polymer network. Top: polymer network structure, showing all sites in the CG model. Bottom: network graph representation, with vertices corresponding to all reactive sites and edges corresponding to the bond connections between them.

data were normalized so that a probability density function is recovered (i.e. the integral of the histogram is unity). The MCC distributions are broad at low conversions, indicating relatively long chain segments between cross-links; as the reaction proceeds to completion, the distributions narrow, corresponding to the formation of cross-links that bridge the polymer chains at more frequent spatial intervals. The MCC histograms contain a rich variety of information regarding the polymer bond topology; for example, a minimium closed cycle value of 2 corresponds to 'back-biting' reactions, where a monomer end group binds to the other end group of the same monomer. Surprisingly, for all conversion values, there are no significant differences noted in the MCC histograms as a function of K_a. This is confirmed in figure 3.27, which shows the MCC distributions for fixed conversions of 90% as a function of various parameters.

Recall that values of $K_a \to 1$ correspond to traditional radical polymerization (TRP), whereas values of $K_a \ll 1$ correspond to controlled radical polymerization (CRP). It therefore appears that for a given conversion, the simulations do not show any appreciable differences in network topology between TRP and CRP, at least as measured by the distributions of minimum closed cycles. We have also analyzed the distribution of all closed cycles, i.e. the length of all paths that return to a given vertex, and also did not find any differences (data not shown).

Experimental attempts to quantify network topology were challenging, as discussed in section 3, and it is not clear what differences, if any, are seen experimentally between TRP and CRP samples. However, the mechanical properties discussed in section 3 do show some

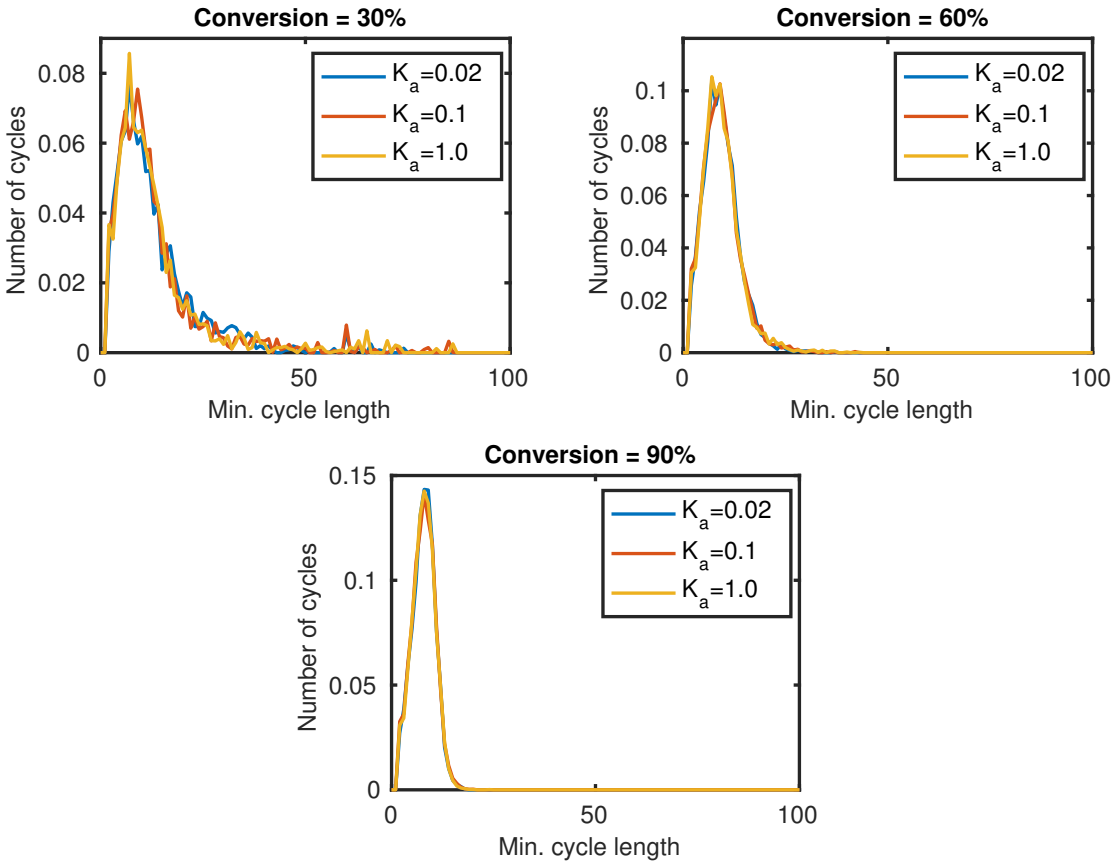

Figure 3.27. Distributions of minimum cycle lengths at various conversions. For all cases, $x_i = 0.00625$ and $N_r = N_a = 1000$.

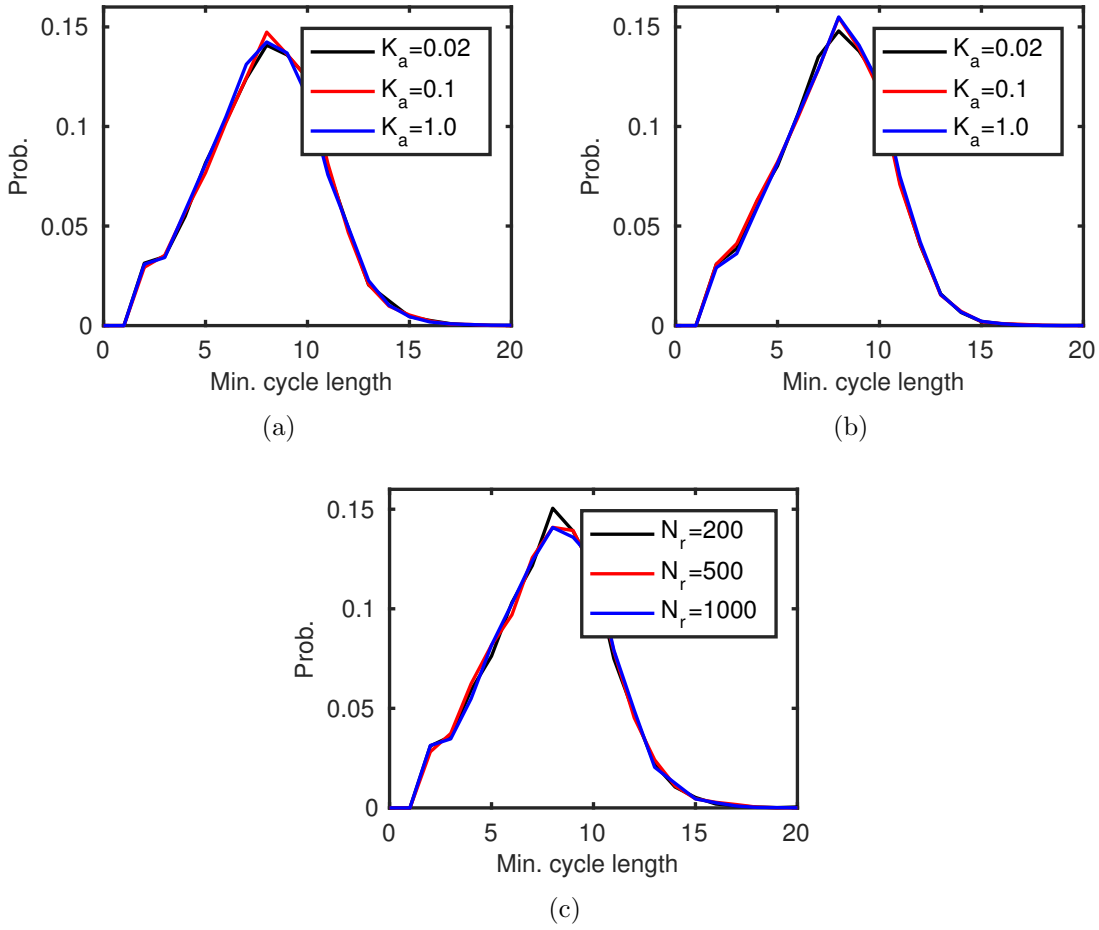

Figure 3.28. Distributions of minimum cycle lengths for various parameter choices. (a): Conversion of 90%, $x_i = 0.00625, N_r = 1000, N_a = 10,000$. (b): Conversion of 95%, $x_i = 0.00625, N_r = 1000, N_a = 10,000$ and larger system of 36,000 monomers. (c): Conversion of 90%, $x_i = 0.00625, K_a = 0.02, N_a = 1,000$, various N_r values. In all cases, minimum cycle distributions show no appreciable differences.

differences in both elongation at failure and elastic moduli between TRP and CRP, which presumably are caused by underlying differences in network topology. For UDMA, significant differences in mechanical properties are seen at all temperatures between as-cured TRP and CRP samples (see figure 3.12); however, as discussed earlier (see table 3), the CRP samples in this case correspond to significant lower conversions, so that differences in mechanical properties are not surprising (the simulations likewise show differences in network topology at different conversions, see figure 3.27). After post-curing, which brings the conversion of TRP and CRP samples to the same levels ($\approx 95\%$), differences in mechanical properties of UDMA samples appear to largely disappear (see table 3). This is qualitatively consistent with the network topology measurements in simulations, which show no differences between TRP and CRP for equal conversion values. Interestingly, the differences in the BisGMA/TEGDMA TRP and CRP samples persist even after post-curing (figure 3.15 and table 3); however, given the fundamental differences in the chemistry of the UDMA and BisGMA/TEGDMA systems, a comparison to simulations (which are based exclusively on UDMA) may not be relevant.

Mechanical properties from CG simulations

To facilitate a more direct comparison to experiments, we performed molecular dynamics to measure the mechanical properties of the structures formed above. Calculations were performed for 3 different values of K_a and different values of conversion. We calculated elastic moduli by deforming the simulation cell (at each conversion, polymerization was stopped during the course of the mechanical deformation simulation). In particular, the Young's modulus is obtained by increasing the x length of the cell at a constant strain rate while expanding the y and z lengths to keep the total volume constant.

The strain rate used ($1 \cdot 10^{-5}$) is slow enough to be in the linear response regime. We calculate the stress tensor and obtain Young's modulus E from the slope of the P_{xx} vs strain curve. The uncertainty in the individual E is large in comparison to the differences in E between different networks. This uncertainty reflects the system size and could be reduced by performing much larger simulations, but that would be much more computationally expensive. However, the variation in E plotted in figure 3.29, particularly for $K_a = 1.0$ is such that no discernible trend can be found as a function of K_a or conversion.

After some thought, we consider this result to be expected because of the nature of the model used. The particle-particle interactions are primarily non-bonded LJ interactions and the modulus simulation is basically probing the effect of small strains on the network which change the separation of the LJ particles. Thus the stress is the sum of LJ forces and is primarily just measuring the Young's modulus of a comparable LJ glass. Note that the bonds are not stretched at these low strains. Thus there is not a discernible effect of the different network structures. This indicates a weakness in the model with respect to the actual thermoset polymers. We are missing relevant details of the atomistic interactions for the cross-linked systems, which is a ripe area for future work. While there are some issues of concern with performing atomistic simulations such as the quality of the force-field,

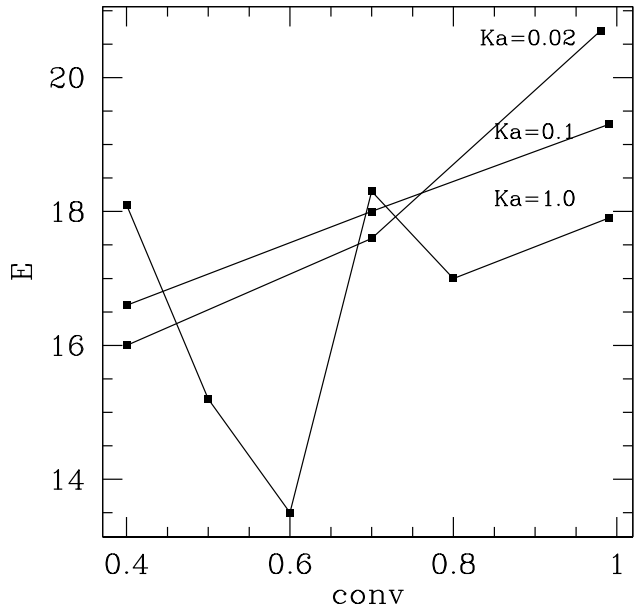

Figure 3.29. Young's modulus E as a function of conversion and K_a

only small systems would be needed to examine the deformations and determine if there are interactions that lead to qualitatively different behavior from the coarse-grained model. Thus, a future direction is to calculate the moduli using atomistic MD, and to understand the connection between the molecular structure and the elastic moduli. This result would help design a better coarse-grained model that would incorporate the key features for the mechanical response.

Chapter 4

Conclusions

Samples of both UDMA and 70/30 BisGMA/TEGDMA were successfully synthesized using both traditional (TRP) and controlled (CRP) radical polymerization strategies in each case. The cure kinetics were quantified using FTIR and DSC. Accurate determination of the extent of cure was essential, and this was achieved using a combination of near-FTIR based on the 6165 cm^{-1} band and NMR, two techniques that showed strong quantitative agreement. The extent of cure was measured as a function of polymer chemistry (UDMA vs. BisGMA/TEGDMA), polymerization scheme (CRP vs. TRP) and cure temperature. With regard to kinetics, the expected differences between TRP and CRP systems were observed, where TRP systems showed significantly faster kinetics in all cases. The final cure was generally lower for CRP systems; in order to facilitate a direct comparison between TRP and CRP systems at comparable values of conversion, samples were also post-cured above T_g to reach nearly complete conversion in all cases ($\geq 94\%$).

In conjunction with the experimental investigations, this work developed a novel coarse-grained (CG) molecular dynamics model of the polymerization reaction that accounts for the controlled nature of the ATRP reaction. To our knowledge, this is the first model that explicitly includes the activation/deactivation reactions. Given the limited time of the project, we focused simulation efforts on the UDMA system, as this avoids the complication of multiple monomer species, which requires additional parameters. Fully atomistic simulations of UDMA monomers demonstrated the importance of accurately capturing the monomer flexibility characteristics, and we calibrated CG parameters based on the results of atomistic simulations. The CG reacting simulations produce qualitatively correct kinetics when compared to experiments, with the important exception that the final conversions are always very high; this may be an indication of a shortcoming in the model, where the regime of diffusion-limited kinetics at high conversions is not adequately captured, or termination reactions are not sufficiently frequent. Future simulation work in this area is needed to investigate these issues.

Mechanical performance was investigated experimentally using three-point bend tests. As-cured samples of UDMA showed significant differences between TRP and CRP samples, with the latter showing both lower moduli and larger strains at failure (in many cases, failure was not observed at the maximum achievable strain). However, these differences largely disappear with post-curing of the samples, which brings both CRP and TRP samples to the same high conversion ($\approx 95\%$). Thus, the differences in mechanical performance in the

case of UDMA appear to be caused by differences in conversion rather than polymerization scheme. Cross-linked structures generated by simulations of UDMA were analyzed using techniques from graph theory to quantify network heterogeneity. For the same conversion, no significant differences in bond network topology between TRP and CRP simulations were observed, consistent with the experiments. Interestingly, the simulations did suggest a heterogeneous network topology at low conversion, which becomes increasingly homogeneous at high conversion. This may be consistent with the experimental observations of increased ductility (as measured by elongation at failure) at low conversion, which diminishes with increasing conversion. Experimental investigations of network heterogeneity were attempted by a wide range of techniques (DSC, NMR, AFM, XRD and SAXS), but quantitative results are difficult to interpret.

It appears that the simulations are therefore consistent with the experimental results for UDMA systems, in that there are no significant differences in mechanical properties or network heterogeneity as measured experimentally between TRP and CRP, and no differences in network topology as measured from simulations, as long as the comparison is made for the same conversion. The more interesting case experimentally is the BisGMA/TEGDMA system, where notable differences in mechanical properties between CRP and TRP persist even for equal conversion values; future simulation work should therefore likely focus on this more complex system. However, there is also the possibility that the simulation model fundamentally fails to capture the features of the experimental systems that lead to differences in network topology and mechanical properties. These limitations may be a result of an inadequate ratio between the monomer diffusion and reaction kinetics timescales, as well as the relatively simple nature of the monomer structure and the polymerization mechanism. The insensitivity of the mechanical properties measured from simulations to cure extent suggest that more detailed CG or fully atomistic simulations may be needed for these systems.

The work presented here has achieved the goal of demonstrating the use of controlled radical polymerization to enhance the mechanical performance of a thermoset polymer in the case of the BisGMA/TEGDMA system. Novel simulation methods were developed and demonstrated for the analysis of these systems, but important fundamental questions remain with regard to the connection between polymer chemistry, cross-link network topology and mechanical properties. This project has demonstrated this to be an area ripe for future work both in terms of fundamental scientific study and applications, with important implications for the development of enhanced thermosetting materials for coatings, underfills and encapsulants.

References

[1] M. L. Arias, P. M. Frontini, and R. J. J. Williams. Analysis of the damage zone around the crack tip for two rubber-modified epoxy matrices exhibiting different toughenability. *Polymer*, 44:1537–1546, 2003.

[2] R. Bagheri, B. Marouf, and R. A. Pearson. Rubber-Toughened Epoxies: A Critical Review. *Polymer Reviews*, 49:201–225, 2009.

[3] I. M. Barszczewska-Rybarek. Structure-property relationships in dimethacrylate networks based on bis-gma, udam and tegdma. *Dental Materials*, 25:1082–1089, 2009.

[4] R. S. Bauer. *183rd Meeting of the American Chemical Society, Las Vegas, Nevada, March 28April 2, 1982*, pages ix–x. American Chemical Society, Washington, D. C., 1983.

[5] Norman Biggs. *Algebraic graph theory*. Cambridge university press, 1993.

[6] J. S. Chen and T. L. Yu. Microgelation of unsaturated polyester resins by static and dynamic light scattering. *Journal of Applied Polymer Science*, 69:871–878, 1998.

[7] K. Chenoweth, S. Cheung, A. CT Van Duin, W. A Goddard, and E. M Kober. Simulations on the thermal decomposition of a poly (dimethylsiloxane) polymer using the reaxff reactive force field. *Journal Of The American Chemical Society*, 127(19):7192–7202, 2005.

[8] K. Chenoweth, A. C. T. van Duin, and W. A.Goddard III. ReaxFF reactive force field for molecular dynamics simulation of hydrocarbon oxidation. *J. Phys. Chem. A*, 112:1040, 2008.

[9] P. Debye, H. R. Jr. Anderson, and H. Brumberger. Scattering by an Inhomogeneous Solid. II. The Correlation Function and Its Application. *Journal of Applied Physics*, 28:679–683, 1957.

[10] C. Declet-Perez. *Toughness in block copolymer modi*

ed epoxies. PhD thesis, University of Minnesota, 2014.

[11] P. Deglmann, A. Schäfer, and Christian Lennartz. Application of quantum calculations in the chemical industry-an overview. *International Journal of Quantum Chemistry*, 115(3):107–136, 2015.

[12] R. A. Dickie, Labana S. S., and R. S. Bauer, editors. *Cross-Linked Polymers Chemistry, Properties, and Applications*. American Chemical Society, Washington, D. C., 1988.

[13] P. J. Flory. "molecular size distribution in three dimensional polymers. i. gelation1". *Journal of the American Chemical Society*, 63:3083–3090, 1941.

[14] P. J. Flory. Molecular Size Distribution in Three Dimensional Polymers. II. Trifunctional Branching Units. *Journal of the American Chemical Society*, 63:3091–3096, 1941.

[15] P. J. Flory. Molecular Size Distribution in Three Dimensional Polymers. III. Tetrafunctional Branching Units. *Journal of the American Chemical Society*, 63:3096–3100, 1941.

[16] P. J. Flory. *Principles of Polymer Chemistry.* Cornell University Press, Ithaca, NY, 1953.

[17] Haifeng Gao, Piotr Polanowski, and Krzysztof Matyjaszewski. Gelation in living copolymerization of monomer and divinyl cross-linker: Comparison of atrp experiments with monte carlo simulations. *Macromolecules*, 42(16):5925–5932, 2009.

[18] Alexey A Gavrilov, Pavel V Komarov, and Pavel G Khalatur. Thermal properties and topology of epoxy networks: A multiscale simulation methodology. *Macromolecules*, 48(1):206–212, 2014.

[19] Jan Genzer. In silico polymerization: Computer simulation of controlled radical polymerization in bulk and on flat surfaces. *Macromolecules*, 39(20):7157–7169, 2006.

[20] A. H. Gilbert and C. B. Bucknall. Epoxy resin toughened with thermoplastic. *Makromolekulare Chemie. Macromolecular Symposia*, 45:289–298, 2011.

[21] D. Greszta and K. Matyjaszewski. Mechanism of controlled/"living" radical polymerization of styrene in the presence of nitroxyl radicals. kinetics and simulations. *Macromolecules*, 29(24):7661–7670, 1996.

[22] J. Hafner. Ab-initio simulations of materials using vasp: Density-functional theory and beyond. *Journal of computational chemistry*, 29(13):2044–2078, 2008.

[23] J. He, H. Zhang, J. Chen, and Y. Yang. Monte carlo simulation of kinetics and chain length distributions in living free-radical polymerization. *Macromolecules*, 30(25):8010–8018, 1997.

[24] D. R. Heine, G. S. Grest, C. D. Lorenz, M. Tsige, and M. J. Stevens. Atomistic simulations of end-linked poly (dimethylsiloxane) networks: structure and relaxation. *Macromolecules*, 37(10):3857–3864, 2004.

[25] N. Ide and T. Fukuda. Nitroxide-Mediated Free-Radical Copolymerization of Vinyl and Divinyl Monomers. Evaluation of Pendant-Vinyl Reactivity. *Macromolecules*, 30:4268–4271, 1997.

[26] N. Ide and T. Fukuda. Nitroxide-Controlled Free-Radical Copolymerization of Vinyl and Divinyl Monomers. 2. Gelation. *Macromolecules*, 32:95–99, 1999.

[27] Pieter J. in 't Veld and Gregory C. Rutledge. Temperature-dependent elasticity of a semicrystalline interphase composed of freely rotating chains. *Macromolecules*, 36(19):7358–7365, 2003.

[28] J. Jancar, W. Wang, and A. T. Dibenedetto. On the heterogenous structure of thermally ccure bis-GMA/TEGDMA resins. *Journal of Materials Science: Materials in Medicine*, 11:675–682, 2000.

[29] C. Jiang, Y. Shen, S. Zhu, and D. Hunkeler. Gel Formation in Atom Transfer Radical Polymerization of 2-(N,N-Dimethylamino)ethyl Methacrylate and Ethylene Glycol Dimethacrylate. *Journal of Polymer Science, Part A: Polymer Chemistry*, 39:3780–3788, 2001.

[30] W. L. Jorgensen, J. D. Madura, and C. J. Swenson. *J. Am. Chem. Soc.*, 106:6638, 1984.

[31] W. L. Jorgensen, D. S. Maxwell, and J. Tirado-Rives. *J. Am. Chem. Soc.*, 118:11225, 1996.

[32] W. L. Jorgensen, D. S. Maxwell, and J. Tirado-Rives. Development and testing of the opls all-atom force field on conformational energetics and properties of organic liquids. *Journal of the American Chemical Society*, 118(45):11225–11236, 1996.

[33] M. R. Kamal. Thermoset Characterization for Moldability Analysis. *Polymer Engineering and Science*, 14:231–239, 1974.

[34] M. Kato, M. Kamigaito, M. Sawamoto, and T. Higashimura. Polymerization of Methyl Methacrylate with the Carbon Tetrachloride/Dichlorotris- (triphenylphosphine)ruthenium(II)/Methylaluminum Bis(2,6-di-tert-butylphenoxide) Initiating System: Possibility of Living Radical Polymerization. *Macromolecules*, 28:1721–1723, 1995.

[35] S. C. Lignon-Auer, M. Schwentenwein, C. Gorsche, J. Stampfl, and R. Liska. Toughening of photo-curable polymer networks: a review. *Polymer Chemistry*, 7:257–286, 2016.

[36] Erlita Mastan, Xiaohui Li, and Shiping Zhu. Modeling and theoretical development in controlled radical polymerization. *Progress in Polymer Science*, 45:71–101, 2015.

[37] G. Moad, E. Rizzardo, and S. H. Thang. Radical addition-fragmentation chemistry in polymer synthesis. *Polymer*, 49:1079–1131, 2008.

[38] A. HE Mueller, D. Yan, G. Litvinenko, R. Zhuang, and H. Dong. Kinetic analysis of "living" polymerization processes exhibiting slow equilibria. 2. molecular weight distribution for degenerative transfer (direct activity exchange between active and" dormant" species) at constant monomer concentration. *Macromolecules*, 28(22):7335–7338, 1995.

[39] J. Nicolas, Y Guillaneuf, C. Lefay, D. Bertin, D. Gigmes, and B. Charleux. Nitroxide-mediated polymerization. *Progress in Polymer Science*, 38:63–235, 2013.

[40] George Odian. *Principles of Polymerization: Fourth Edition.* John Wiley & Sons, Inc., 2004.

[41] J. P. Pascault, H. Sautereau, J. Verdu, and R. J. J. Williams. *Thermosetting Polymers*. Marcel Dekker: New York, 2002.

[42] T. Pintauer and K. Matyjaszewski. Atom transfer radical addition and polymerization reactions catalyzed by ppm amounts of copper complexes. *Chemical Society Reviews*, 37:1087–1097, 2008.

[43] S. Plimpton. Fast parallel algorithms for short-range molecular dynamics. *Journal of computational physics*, 117(1):1–19, 1995.

[44] G. Porod. Die röntgenkleinwinkelstreuung von dichtgepackten kolloiden systemen. *Kolloid-Zeitschrift*, 124:83–114, 1951.

[45] E. M. Redline, L. F. Francis, and F. S. Bates. Radical-Cured Block Copolymer-Modified Thermosets. *Journal of Polymer Science, Part B: Polymer Physics*, 49:540–550, 2011.

[46] D. E. Roberts. Heats of Polymerization. A Summary of Published Values and Their Relation to Structure. *Journal of Research of the National Bureau of Standards*, 44:221–232, 1950.

[47] E. Rodriguez, M. Larrañaga, I. Mondragón, and A. Vázquez. Relationship between the network morphology and properties of commercial vinyl ester resins. *Journal of Applied Polymer Science*, 100:3895–3903, 2006.

[48] C. M. Roome and C. D. Adam. Crystallite orientation and anisotropic strains in thermally sprayed hydroxyapatite coatings. *Biomaterials*, 16:691–696, 1995.

[49] L. Ruiz-Pérez, G. J. Royston, J. P. A. Faircough, and A. J. Ryan. Toughening by nanostructure. *Polymer*, 49:4475–4488, 2008.

[50] W. H. Stockmayer. "theory of molecular size distribution and gel formation in branched-chain polymers". *Journal of Chemical Physics*, 11:45–55, 1943.

[51] W. H. Stockmayer. "theory of molecular size distribution and gel formation in branched polymers ii. general cross linking". *Journal of Chemical Physics*, 12:125–131, 1944.

[52] A. CT Van Duin, S. Dasgupta, F. Lorant, and W. A. Goddard. Reaxff: a reactive force field for hydrocarbons. *The Journal of Physical Chemistry A*, 105(41):9396–9409, 2001.

[53] Adri C. T. van Duin, Siddharth Dasgupta, Francois Lorant, and William A. Goddard III. *J. Phys. Chem. A*, 105:9396, 2001.

[54] J-S Wang and K. Matyjaszewski. Controlled/"living" radical polymerization. atom transfer radical polymerization in the presence of transition-metal complexes. *Journal of the American Chemical Society*, 117:5614–5615, 1995.

[55] J. H. Ward, A. Shahar, and N. A. Peppas. Kinetics of 'living' radical polymerization of multifunctional monomers. *Polymer*, 43:1745–1752, 2002.

[56] I. Yarovsky and E. Evans. Computer simulation of structure and properties of crosslinked polymers: application to epoxy resins. *Polymer*, 43(3):963–969, 2002.

[57] Xin Yong, Olga Kuksenok, and Anna C Balazs. Modeling free radical polymerization using dissipative particle dynamics. *Polymer*, 72:217–225, 2015.

[58] Xin Yong, Olga Kuksenok, Krzysztof Matyjaszewski, and Anna C Balazs. Harnessing interfacially-active nanorods to regenerate severed polymer gels. *Nano letters*, 13(12):6269–6274, 2013.

[59] Q. Yu, F. Zeng, and S. Zhu. Atom Transfer Radical Polymerization of Poly(ethylene glycol) Dimethacrylate. *Macromolecules*, 34:1612–1618, 2001.

[60] Q. Yu, M. Zhou, Y. Ding, B. Jiang, and S. Zhu. Development of networks in atom transfer radical polymerization of dimethacrylates. *Polymer*, 48:7058–7064, 2007.

[61] Min Zhang and W Harmon Ray. Modeling of living free-radical polymerization processes. i. batch, semibatch, and continuous tank reactors. *Journal of applied polymer science*, 86(7):1630–1662, 2002.

[62] Shiping Zhu. Modeling of molecular weight development in atom transfer radical polymerization. *Macromolecular theory and simulations*, 8(1):29–37, 1999.

Appendix A

Additional Experimental Data

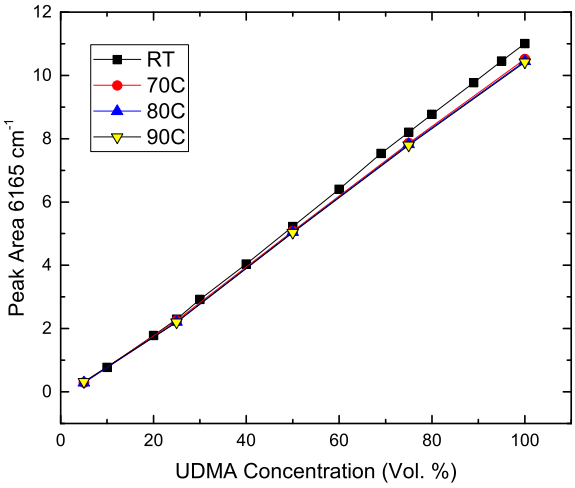

Figure A.1. UDMA NIR calibration curves.

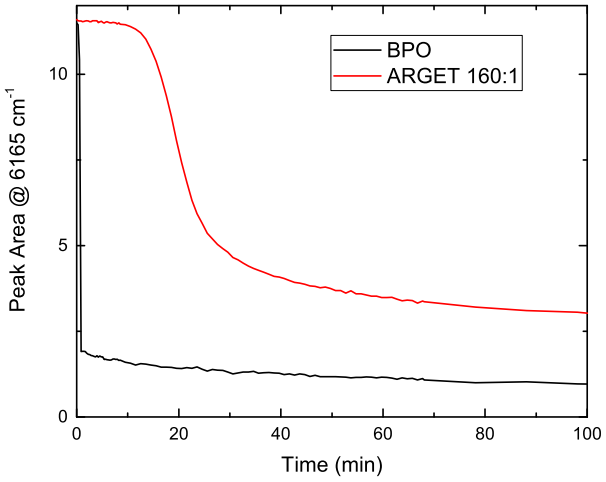

Figure A.2. UDMA NIR methacrylate peak area versus time at 90 °C for TRP (black) and CRP (red).

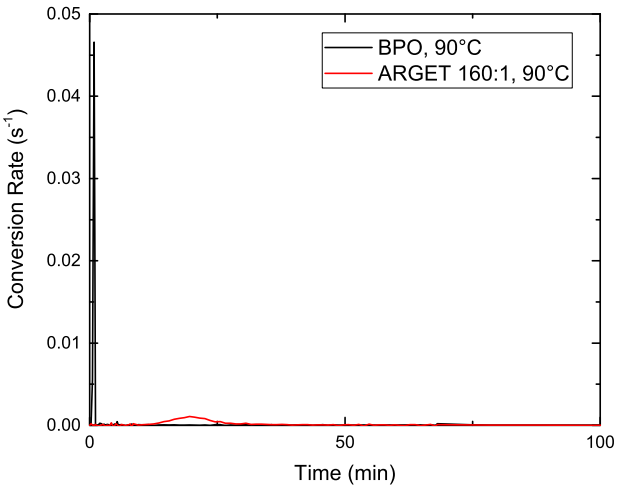

Figure A.3. UDMA polymerization rate determined using NIR 90 °C for TRP (black) and CRP (red).

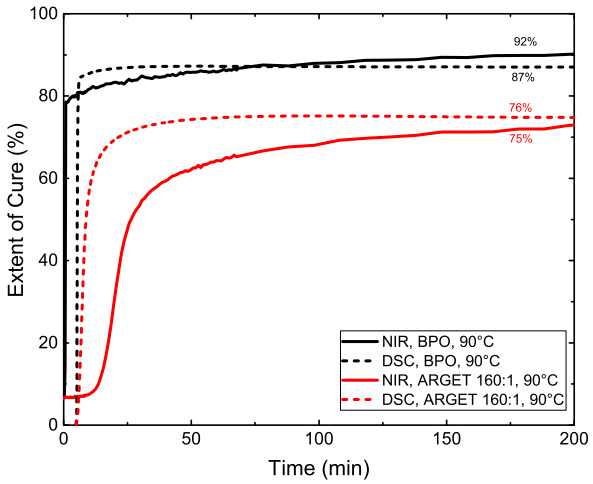

Figure A.4. A comparison NIR and DSC extent of cure versus time plots for UDMA cured at 90 °C. NIR data is presented in solid lines while DSC are represented by dashed lines. TRP lines are black while CRP lines are red.

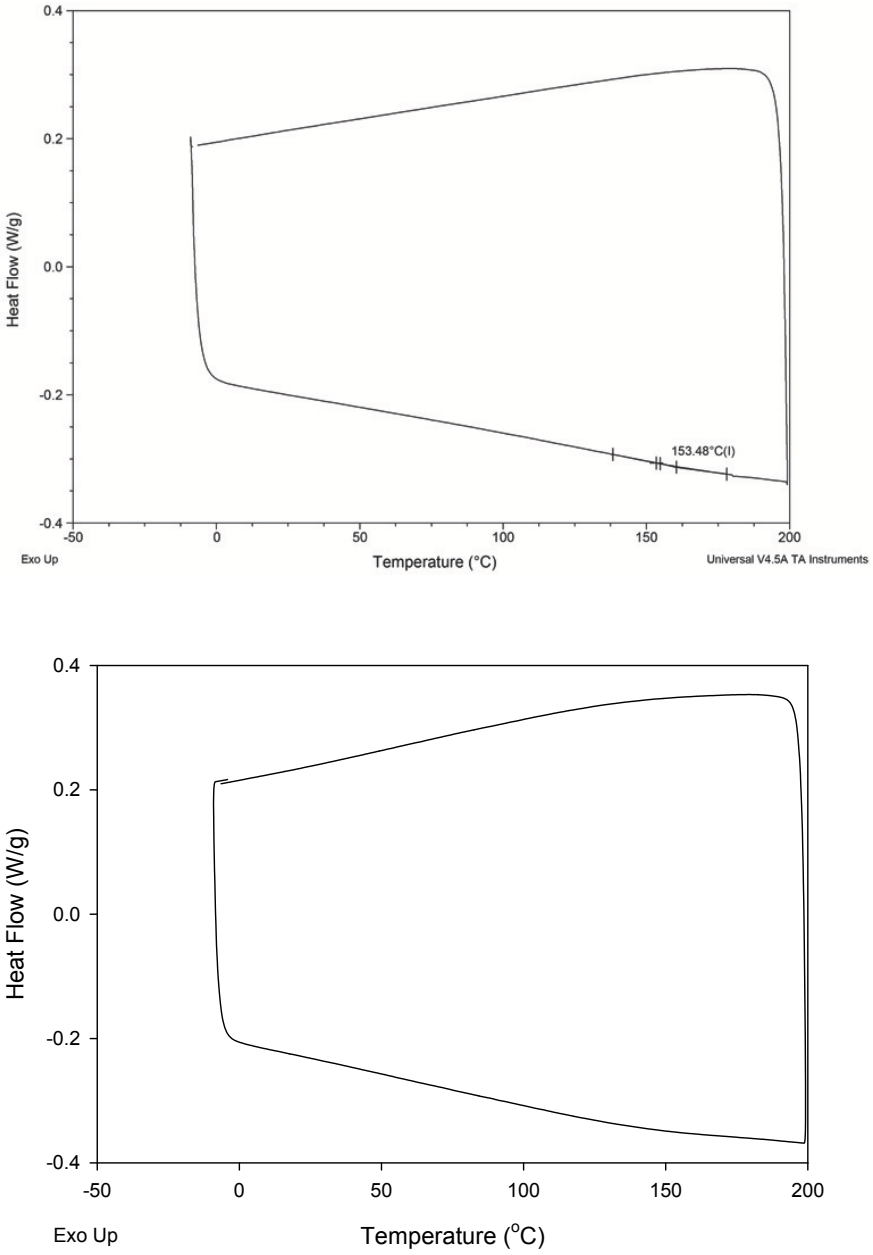

Figure A.5. DSC trace of BisGMA/TEGDMA 70/30 w/w cured with benzoyl peroxide (top) and CRP (bottom) at 90 °C. The glass transition temperature appears to be around 154 °C for the TRP cure but was not easily discernible from the DSC traces for the CRP cure.

Appendix B

Additional simulation data

B.1 Five-site coarse grained representation of UDMA

Figure B.1 shows visual representations of the reacting system in the base case ($x_i = 0.00635, K_a = 0.1, N_r = 1000, N_a = 1000$). Conversion here and in all subsequent discussion is defined as the fraction of reacted end groups divided by the total number of end groups In the top panel of Figure B.1, each polymer chain is assigned a different color. At low conversion, several polymer chains have formed, seeded by the radical groups that were initialized at the start of the simulations (although a fraction $1 - K_a$ of these are initially inactive, they are eventually activated and chain growth begins). Once the smaller chains merge, a single large, percolating chain is dominant, as there is no mechanism for starting additional chains. At that point, the reaction continues by addition of monomers to the existing percolating network. In the bottom panel of Figure B.1, polymer chains are colored by size, with red representing the smallest chains (monomers), white representing medium-sized chains, and blue representing the largest chain (the percolated network at the end of the simulation). The same trend is also apparent in this visualization, where the reaction quickly leads to the formation of a percolating network, which grows by addition of monomers to span the entire system.

Figure B.2 shows the evolution of the overall system density as the reaction proceeds, both as a function of simulation time and conversion. As above, only the base case is shown here. The absolute density value is currently not meaningful, as it relates only to the length scale set by the coarse-grained simulation units (σ); we therefore only discuss the change in density ρ relative to the initial density ρ_0. As expected, an increase in density is observed as the reaction proceeds, in this case of $\sim 25\%$. This can be explained as the result of bond formation, leading to closer and more ordered packing of monomers. The same effect is observed experimentally.

Figures B.3 to B.6 show the effects of the key parameters identified above on the overall reaction kinetics. The same base case discussed above ($x_i = 0.00635, K_a = 0.1, N_r = 1000, N_a = 1000$) is modified one parameter at a time, with all other parameters retaining their base case values. In all cases, the reaction proceeds to nearly 100% conversion. This is somewhat in disagreement with experiments, where conversions $\sim 90\%$ are more typical. While this is not a major cause for concern, there are several factors that can explain this

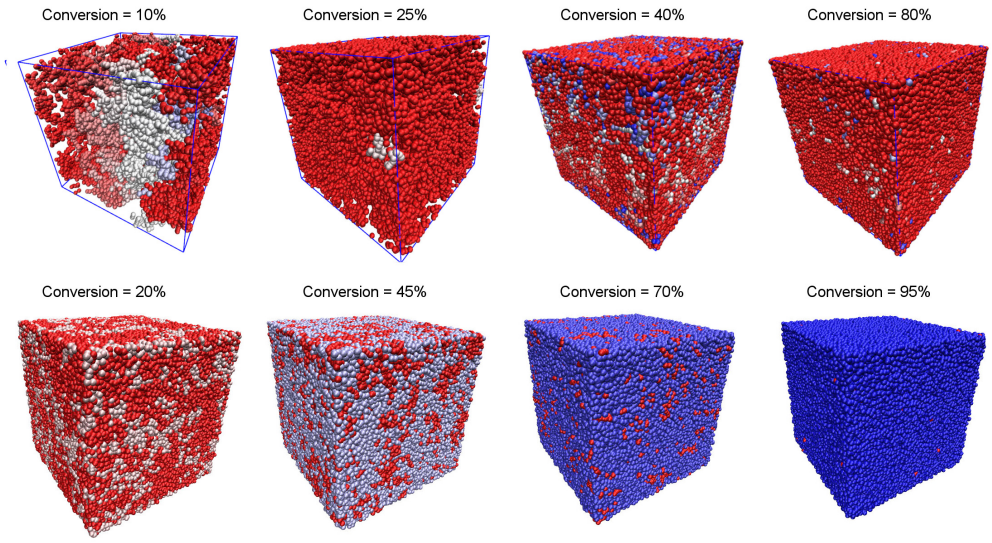

Figure B.1. Visualization of the simulation system as the reaction proceeds. Top: individual chains are assigned a different color. For clarity, monomers are omitted at 10% and 25% conversion, but shown for the other cases. Bottom: Polymer chains (including monomers) are colored by size, with an increase in size corresponding to a transition from red to pink to white to light blue to dark blue.

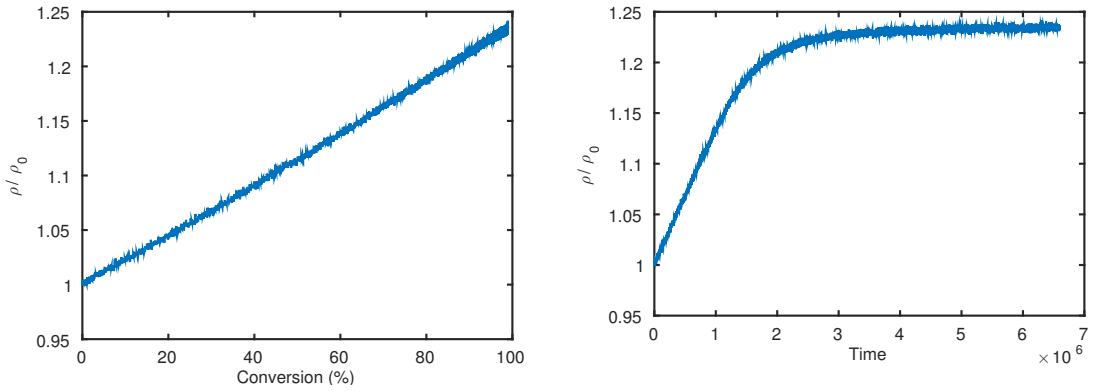

Figure B.2. Change in overall system density as a function of extent of reaction

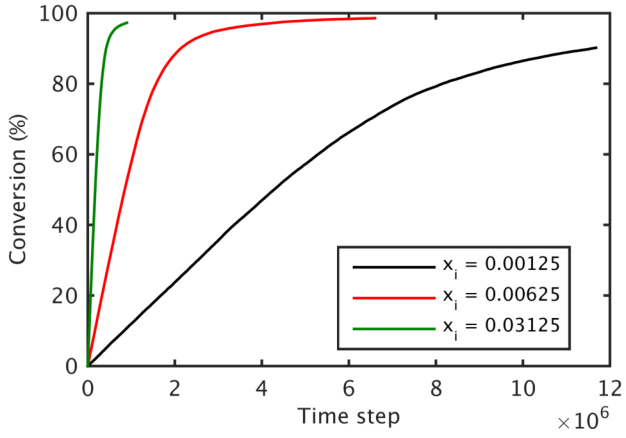

Figure B.3. Effects of initiator concentration x_i on reaction kinetics

discrepancy. For example, the simple five-bead structure of the monomers in coarse-grained simulations renders them relatively mobile even in a highly cross-linked network, whereas a more complex structure (e.g. UDMA) would be sterically inhibited and more prone to entanglement. This can likely be compensated for by either increasing the number of beads, or adjusting the simulation temperature to decrease overall diffusion. Additionally, the reaction criterion in the simulations only takes into account distance between reacting groups, whereas relative orientation also plays an important role in the experimental system.

Figure B.3 shows the effect of the initiator concentration x_i on the reaction kinetics. Not surprisingly, a higher concentration leads to faster kinetics, since more chains are reacting. The fast reaction at short times followed by a slow progression to complete conversion is more characteristic of traditional radical polymerization, which is the expected limit for a high concentration of initiator. The effects of K_a (Figure B.4) are similar, where a high value of K_a, which translates to larger fraction of radicals being active, leads to a shift towards the fast early kinetics followed by a slower plateau. In contrast, a smaller value of K_a corresponds to a near-linear conversion curve. In the limit $K_a = 1$, the traditional radical polymerization reaction mechanism is recovered. Overall this is the expected behavior, and the canonical difference in kinetics between traditional and controlled radical polymerization is thus well-reflected in these results.

Figure B.5 shows the effects of the relative elongation reaction rate on conversion kinetics. Recall that N_r is defined as the number of simulation steps between attempts to carry out an elongation step, so that a smaller vaue of N_r corresponds to a shorter timescale of the elongation reaction. Clearly, the overall kinetics increase with decreasing N_r. While this may be an obvious effect, the importance of N_r is in relation to the timescale of diffusion. At large N_r values, small chains are expected to undergo more extensive diffusion and relaxation before their next elongation, potentially leading to systems with lower residual stresses in

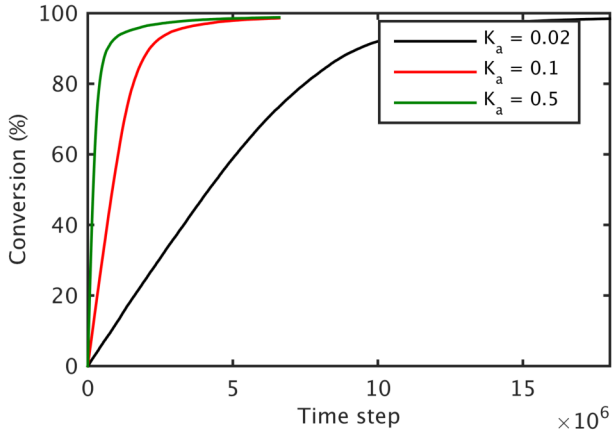

Figure B.4. Effects of activation/deactivation reaction equilibrium K_a on reaction kinetics

the polymer network, which has important implications for mechanical properties.

Finally, Figure B.6 shows the effect of the radical activation/deactivation reaction time scale, where again a lower value of N_a corresponds to more frequent attempts at switching radical states. Clearly, there is no significant effect of N_a on overall reaction kinetics in the range of values tested. This simply reflects that the reaction is limited only by the kinetics of elongation and the total, rather than local availability of active radicals. In a situation where diffusion of monomers to active radical sites becomes limiting, one might expect N_a to have a more significant effect, but that is not the case here. However, while the overall kinetics appear unaffected, there are almost certainly local effects on the network topology that are important for mechanical behavior.

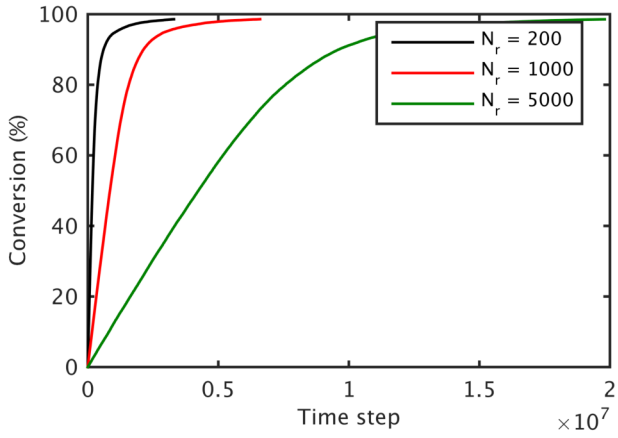

Figure B.5. Effects of reaction time scale N_r on reaction kinetics

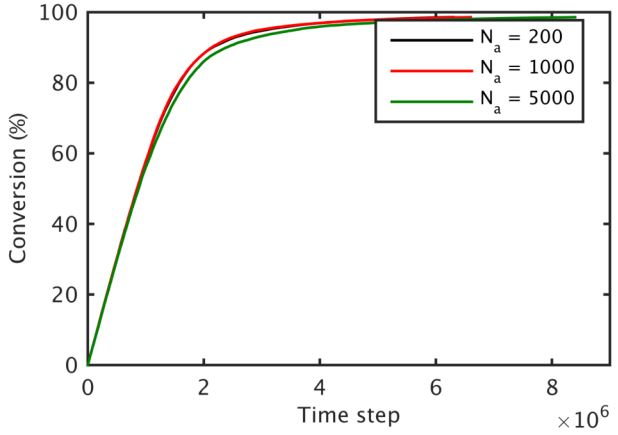

Figure B.6. Effects of activation/deactivation time scale N_a on reaction kinetics

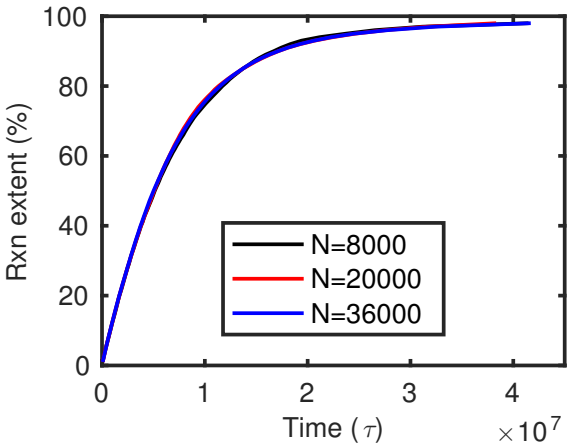

Figure B.7. Overall reaction kinetics as a function of numer of monomers in the simulation domain

B.2 Additional data for seven-site coarse-grained model of UDMA

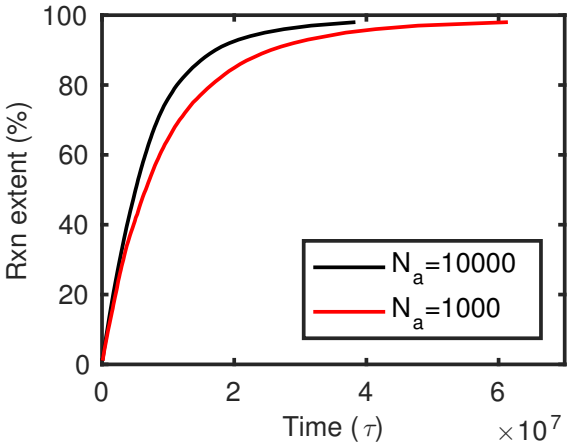

Figure B.8. Overall reaction kinetics as a function of N_a, the number of simulation time steps between activation/deactivation events.

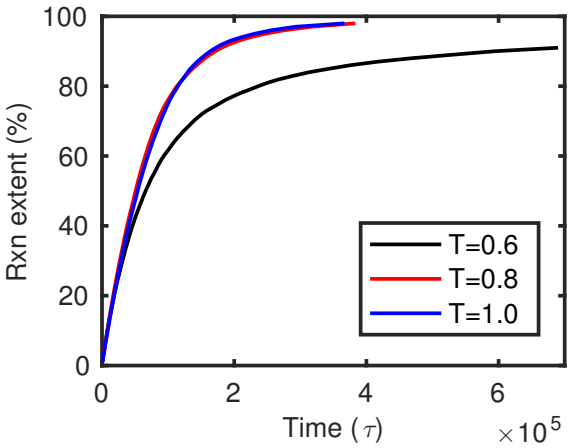

Figure B.9. Overall reaction kinetics as a function of simulation temperature.

B.3 OPLS potential parameter file for atomistic simulations of UDMA

```
# LAMMPS parameters created by EMC v9.3.8, build Mar 25 2015 07:50:47

# Masses

mass 1   12.01100  # ct
mass 2    1.00790  # hc
mass 3   12.01100  # cm
mass 4    1.00790  # hc1
mass 5   12.01100  # c
mass 6   15.99940  # o
mass 7   15.99940  # os1
mass 8   14.00670  # n_1
mass 9    1.00790  # h

# Potentials

pair_style lj/cut/coul/long ${cutoff} ${charge_cutoff}  # 9.5
bond_style harmonic
angle_style harmonic
dihedral_style multi/harmonic
special_bonds lj/coul 0 0 0.5

# Pair Coeffs

pair_coeff  1  1    0.06600    3.50000  # ct,ct
pair_coeff  2  2    0.03000    2.50000  # hc,hc
pair_coeff  3  3    0.07600    3.55000  # cm,cm
pair_coeff  4  4    0.03000    2.42000  # hc1,hc1
pair_coeff  5  5    0.10500    3.75000  # c,c
pair_coeff  6  6    0.21000    2.96000  # o,o
pair_coeff  7  7    0.17000    3.00000  # os1,os1
pair_coeff  8  8    0.17000    3.25000  # n_1,n_1
pair_coeff  9  9    0.00000    0.00000  # h,h

# Bond Coeffs

bond_coeff  1  268.00000    1.52900  # ct,ct
bond_coeff  2  340.00000    1.09000  # ct,hc
bond_coeff  3  317.00000    1.51000  # ct,cm
```

```
bond_coeff  4  320.00000    1.41000  # ct,os1
bond_coeff  5  337.00000    1.44900  # ct,n_1
bond_coeff  6  549.00000    1.34000  # cm,cm
bond_coeff  7  340.00000    1.08000  # cm,hc1
bond_coeff  8  410.00000    1.44400  # cm,c
bond_coeff  9  570.00000    1.22900  # c,o
bond_coeff 10  214.00000    1.32700  # c,os1
bond_coeff 11  490.00000    1.33500  # c,n_1
bond_coeff 12  434.00000    1.01000  # n_1,h

# Angle Coeffs

angle_coeff  1   58.35000  112.70000  # ct,ct,ct
angle_coeff  2   37.50000  110.70000  # ct,ct,hc
angle_coeff  3   50.00000  109.50000  # ct,ct,os1
angle_coeff  4   80.00000  109.70000  # ct,ct,n_1
angle_coeff  5   70.00000  124.00000  # ct,cm,cm
angle_coeff  6   70.00000  119.70000  # ct,cm,c
angle_coeff  7   83.00000  116.90000  # ct,os1,c
angle_coeff  8   50.00000  121.90000  # ct,n_1,c
angle_coeff  9   38.00000  118.40000  # ct,n_1,h
angle_coeff 10   33.00000  107.80000  # hc,ct,hc
angle_coeff 11   35.00000  109.50000  # hc,ct,cm
angle_coeff 12   35.00000  109.50000  # hc,ct,os1
angle_coeff 13   35.00000  109.50000  # hc,ct,n_1
angle_coeff 14   35.00000  120.00000  # cm,cm,hc1
angle_coeff 15   85.00000  120.70000  # cm,cm,c
angle_coeff 16   80.00000  125.30000  # cm,c,o
angle_coeff 17   81.00000  111.40000  # cm,c,os1
angle_coeff 18   35.00000  117.00000  # hc1,cm,hc1
angle_coeff 19   35.00000  119.80000  # c,n_1,h
angle_coeff 20   83.00000  123.40000  # o,c,os1
angle_coeff 21   80.00000  122.90000  # o,c,n_1
angle_coeff 22   81.00000  111.40000  # os1,c,n_1

# Dihedral Coeffs

dihedral_coeff  1    3.56500    5.39300   -9.42000   -2.77600    8.47200  # ct,ct,ct,ct
dihedral_coeff  2    0.15000    0.45000    0.00000   -0.60000    0.00000  # ct,ct,ct,hc
dihedral_coeff  3   -0.18300   -0.64700    0.96200    1.42600    0.00000  # ct,ct,ct,n_1
dihedral_coeff  4   -0.52500   -1.24300    0.12600    0.84400    0.00000  # ct,ct,os1,c
dihedral_coeff  5   -0.63500   -0.09500    1.42000    0.88000    0.00000  # ct,ct,n_1,c
dihedral_coeff  6    0.00000    0.00000    0.00000    0.00000    0.00000  # ct,ct,n_1,h
dihedral_coeff  7   14.00000    0.00000  -14.00000    0.00000    0.00000  # ct,cm,cm,hc1
dihedral_coeff  8    0.42750    1.20750   -0.23000   -1.01000    0.00000  # ct,cm,c,o
```

```
dihedral_coeff  9    0.42750    1.20750   -0.23000   -1.01000    0.00000  # ct,cm,c,os1
dihedral_coeff 10    7.00000    2.00000   -5.00000    0.00000    0.00000  # ct,os1,c,cm
dihedral_coeff 11    5.12400    0.00000   -5.12400    0.00000    0.00000  # ct,os1,c,o
dihedral_coeff 12    4.00000   -1.00000   -5.00000    0.00000    0.00000  # ct,os1,c,n_1
dihedral_coeff 13    6.08900    0.00000   -6.08900    0.00000    0.00000  # ct,n_1,c,o
dihedral_coeff 14    7.23900    1.15000   -6.08900    0.00000    0.00000  # ct,n_1,c,os1
dihedral_coeff 15    0.15000    0.45000    0.00000   -0.60000    0.00000  # hc,ct,ct,hc
dihedral_coeff 16    0.23400    0.70200    0.00000   -0.93600    0.00000  # hc,ct,ct,os1
dihedral_coeff 17    0.23200    0.69600    0.00000   -0.92800    0.00000  # hc,ct,ct,n_1
dihedral_coeff 18   -0.18600   -0.55800    0.00000    0.74400    0.00000  # hc,ct,cm,cm
dihedral_coeff 19    0.00000    0.00000    0.00000    0.00000    0.00000  # hc,ct,cm,c
dihedral_coeff 20    0.09900    0.29700    0.00000   -0.39600    0.00000  # hc,ct,os1,c
dihedral_coeff 21    0.00000    0.00000    0.00000    0.00000    0.00000  # hc,ct,n_1,c
dihedral_coeff 22    0.00000    0.00000    0.00000    0.00000    0.00000  # hc,ct,n_1,h
dihedral_coeff 23    7.25000    1.25000   -6.00000    0.00000    0.00000  # cm,cm,c,o
dihedral_coeff 24    2.10000    0.00000   -2.10000    0.00000    0.00000  # cm,cm,c,os1
dihedral_coeff 25   14.00000    0.00000  -14.00000    0.00000    0.00000  # hc1,cm,cm,c
dihedral_coeff 26    4.90000    0.00000   -4.90000    0.00000    0.00000  # o,c,n_1,h
dihedral_coeff 27   -0.27500   -0.27500    0.00000    0.00000    0.00000  # os1,ct,ct,os
dihedral_coeff 28    4.90000    0.00000   -4.90000    0.00000    0.00000  # os1,c,n_1,h
```

B.4 UDMA Monomer LAMMPS Data File

```
LAMMPS output created by EMC v9.3.8, build Mar 25 2015 07:50:47

          71  atoms
          70  bonds
         124  angles
         158  dihedrals

           9  atom types
          12  bond types
          22  angle types
          28  dihedral types

             0    9.210613924  xlo xhi
             0    9.210613924  ylo yhi
             0    9.210613924  zlo zhi
#             -25.00    25.00  xlo xhi
#             -25.00    25.00  ylo yhi
#             -25.00    25.00  zlo zhi

Masses

       1    12.0110  # ct
       2     1.0079  # hc
       3    12.0110  # cm
       4     1.0079  # hc1
       5    12.0110  # c
       6    15.9994  # o
       7    15.9994  # os1
       8    14.0067  # n_1
       9     1.0079  # h

Atoms

       1       1   1 -0.1800   7.6762922681   2.1909906383   2.9012299757  # ct
       2       1   2  0.0600   7.0058561885   1.5283001042   3.4414175956  # hc
       3       1   2  0.0600   8.6911918986   1.9929278336   3.2529021212  # hc
       4       1   2  0.0600   7.4283095696   1.8777720428   1.8475003951  # hc
       5       1   3 -0.2300   7.2986625512   3.6303297656   3.0284739831  # cm
       6       1   3  0.0000   7.3448147611   4.3164667442   4.1830633267  # cm
       7       1   4  0.1150   7.1042279580   5.3471566057   4.3486017248  # hc1
       8       1   4  0.1150   7.7661381218   3.8212511014   5.0759642363  # hc1
       9       1   5  0.5100   6.9324884797   4.3924466050   1.8206520271  # c
```

```
10      1   6 -0.4300   7.1205971253   3.9342687601   0.7008544267  # o
11      1   7 -0.3300   5.8326579508   5.1192685205   2.0369286045  # os1
12      1   1  0.1900   5.2164553543   5.9180993174   1.0309609093  # ct
13      1   2  0.0300   5.6588205918   5.9286876537   0.0244445938  # hc
14      1   2  0.0300   5.2880503452   6.8288222845   1.5640153355  # hc
15      1   1  0.1900   3.7226784397   5.6255263410   0.8909802123  # ct
16      1   2  0.0300   3.5661197262   4.5780695703   0.4791373129  # hc
17      1   2  0.0300   3.2456403966   5.6499629261   1.8760751684  # hc
18      1   7 -0.3300   3.0379403481   6.6333424622   0.1083512095  # os1
19      1   5  0.5100   2.0534721132   6.3671465372   8.4789721085  # c
20      1   6 -0.5000   1.2186009352   5.4812700146   8.6403029498  # o
21      1   8 -0.5000   2.0927294905   7.1653238421   7.4392737103  # n_1
22      1   9  0.3000   2.7376154103   7.8952896307   7.3839990768  # h
23      1   1  0.1500   1.1464164283   7.2227002011   6.3455534364  # ct
24      1   2  0.0600   1.0874065653   8.2951536293   6.0640466512  # hc
25      1   2  0.0600   0.1658456139   7.0330482370   6.7488889490  # hc
26      1   1  0.0000   1.5299284219   6.2626043805   5.1248545016  # ct
27      1   1 -0.1800   1.2385639589   4.8401906363   5.6170643986  # ct
28      1   2  0.0600   2.0420954812   4.4936714911   6.2441488426  # hc
29      1   2  0.0600   0.3573533845   4.6741366950   6.1486343218  # hc
30      1   2  0.0600   1.1226543037   4.2200512469   4.7337067414  # hc
31      1   1 -0.1800   0.6246891798   6.5333194299   3.9429760186  # ct
32      1   2  0.0600   0.9372390340   7.3967885300   3.3400496746  # hc
33      1   2  0.0600   8.8669972789   6.8312848783   4.2815460075  # hc
34      1   2  0.0600   0.5040608522   5.7279543257   3.2825635994  # hc
35      1   1 -0.1200   3.0217395403   6.5116642011   4.7178977762  # ct
36      1   2  0.0600   3.3501306375   7.4725990791   5.1978541511  # hc
37      1   2  0.0600   2.9862500255   6.7345739607   3.5904594453  # hc
38      1   1 -0.0600   4.1401289821   5.4029939615   4.8703252178  # ct
39      1   2  0.0600   4.9377626385   5.8121919868   4.2814947593  # hc
40      1   1 -0.1800   3.7792903542   4.0507860172   4.1545328073  # ct
41      1   2  0.0600   3.4319150478   3.2520691768   4.8434698051  # hc
42      1   2  0.0600   3.0039349165   4.1025729546   3.3632091394  # hc
43      1   2  0.0600   4.7067082787   3.6143270375   3.8379214500  # hc
44      1   1 -0.1200   4.8673517268   5.3276545948   6.2085791240  # ct
45      1   2  0.0600   5.8002208680   5.8747772037   6.1856603817  # hc
46      1   2  0.0600   4.2431104141   5.7260978025   7.0036652623  # hc
47      1   1  0.1500   5.3272045885   3.9306833257   6.6775543224  # ct
48      1   2  0.0600   6.3605906528   3.9903556682   7.0080207678  # hc
49      1   2  0.0600   5.2927911158   3.2482919175   5.9020428532  # hc
50      1   8 -0.5000   4.5744032106   3.4084372136   7.8428964671  # n_1
51      1   9  0.3000   4.8163235826   3.9089411804   8.6525851950  # h
52      1   5  0.5100   3.7013235923   2.3978749937   7.8494244638  # c
53      1   6 -0.5000   3.3982503853   1.6998343460   6.8472984796  # o
54      1   7 -0.3300   3.1282632349   2.1785342669   9.0443038673  # os1
```

```
      55       1   1  0.1900   1.9820756400   1.2831354938   9.1976939493  # ct
      56       1   2  0.0300   2.0091935752   0.9540545830   1.0207189597  # hc
      57       1   2  0.0300   2.0663202440   0.4009800356   8.6392144772  # hc
      58       1   1  0.1900   0.6455828462   2.0138902248   9.0043102713  # ct
      59       1   2  0.0300   0.0872102982   2.0697904473   0.7652736437  # hc
      60       1   2  0.0300   0.8634535574   3.0209998741   8.7890721668  # hc
      61       1   7 -0.3300   9.1048969973   1.3775384266   7.9279154659  # os1
      62       1   5  0.5100   8.3239092713   0.3121897147   8.2619634062  # c
      63       1   6 -0.4300   8.4948430017   8.9107688417   0.1241671043  # o
      64       1   3 -0.2300   7.2049602131   0.1555020189   7.2788203441  # cm
      65       1   1 -0.1800   7.0761401055   0.9924978934   6.0467429753  # ct
      66       1   2  0.0600   7.5035733144   0.4620074370   5.2074640253  # hc
      67       1   2  0.0600   7.5446508417   1.9924535945   6.1584677733  # hc
      68       1   2  0.0600   6.0519920633   1.1683003911   5.6909178723  # hc
      69       1   3  0.0000   6.2361750879   8.4418001330   7.5214618876  # cm
      70       1   4  0.1150   5.3933161255   8.2134564576   6.9299723359  # hc1
      71       1   4  0.1150   6.4196961702   7.8002815371   8.4412933108  # hc1

Bonds

       1       3       1       5  # ct,cm
       2       2       1       2  # ct,hc
       3       2       1       3  # ct,hc
       4       2       1       4  # ct,hc
       5       8       5       9  # cm,c
       6       6       5       6  # cm,cm
       7       7       6       7  # cm,hc1
       8       7       6       8  # cm,hc1
       9      10       9      11  # c,os1
      10       9       9      10  # c,o
      11       4      12      11  # ct,os1
      12       1      12      15  # ct,ct
      13       2      12      13  # ct,hc
      14       2      12      14  # ct,hc
      15       4      15      18  # ct,os1
      16       2      15      16  # ct,hc
      17       2      15      17  # ct,hc
      18      10      19      18  # c,os1
      19      11      19      21  # c,n_1
      20       9      19      20  # c,o
      21       5      23      21  # ct,n_1
      22      12      21      22  # n_1,h
      23       1      23      26  # ct,ct
      24       2      23      24  # ct,hc
      25       2      23      25  # ct,hc
```

```
26       1       26      35  # ct,ct
27       1       26      27  # ct,ct
28       1       26      31  # ct,ct
29       2       27      28  # ct,hc
30       2       27      29  # ct,hc
31       2       27      30  # ct,hc
32       2       31      32  # ct,hc
33       2       31      33  # ct,hc
34       2       31      34  # ct,hc
35       1       35      38  # ct,ct
36       2       35      36  # ct,hc
37       2       35      37  # ct,hc
38       1       38      44  # ct,ct
39       1       38      40  # ct,ct
40       2       38      39  # ct,hc
41       2       40      41  # ct,hc
42       2       40      42  # ct,hc
43       2       40      43  # ct,hc
44       1       44      47  # ct,ct
45       2       44      45  # ct,hc
46       2       44      46  # ct,hc
47       5       47      50  # ct,n_1
48       2       47      48  # ct,hc
49       2       47      49  # ct,hc
50      11       52      50  # c,n_1
51      12       50      51  # n_1,h
52      10       52      54  # c,os1
53       9       52      53  # c,o
54       4       55      54  # ct,os1
55       1       55      58  # ct,ct
56       2       55      56  # ct,hc
57       2       55      57  # ct,hc
58       4       58      61  # ct,os1
59       2       58      59  # ct,hc
60       2       58      60  # ct,hc
61      10       62      61  # c,os1
62       8       64      62  # cm,c
63       9       62      63  # c,o
64       6       64      69  # cm,cm
65       3       65      64  # ct,cm
66       2       65      66  # ct,hc
67       2       65      67  # ct,hc
68       2       65      68  # ct,hc
69       7       69      70  # cm,hc1
70       7       69      71  # cm,hc1
```

```
Angles

     1       6       1       5       9  # ct,cm,c
     2       5       1       5       6  # ct,cm,cm
     3      11       2       1       5  # hc,ct,cm
     4      10       2       1       3  # hc,ct,hc
     5      10       2       1       4  # hc,ct,hc
     6      11       3       1       5  # hc,ct,cm
     7      10       3       1       4  # hc,ct,hc
     8      11       4       1       5  # hc,ct,cm
     9      17       5       9      11  # cm,c,os1
    10      16       5       9      10  # cm,c,o
    11      14       5       6       7  # cm,cm,hc1
    12      14       5       6       8  # cm,cm,hc1
    13      15       6       5       9  # cm,cm,c
    14      18       7       6       8  # hc1,cm,hc1
    15       7      12      11       9  # ct,os1,c
    16      20      10       9      11  # o,c,os1
    17       3      15      12      11  # ct,ct,os1
    18      12      13      12      11  # hc,ct,os1
    19      12      14      12      11  # hc,ct,os1
    20       3      12      15      18  # ct,ct,os1
    21       2      12      15      16  # ct,ct,hc
    22       2      12      15      17  # ct,ct,hc
    23       2      15      12      13  # ct,ct,hc
    24      10      13      12      14  # hc,ct,hc
    25       2      15      12      14  # ct,ct,hc
    26       7      15      18      19  # ct,os1,c
    27      12      16      15      18  # hc,ct,os1
    28      10      16      15      17  # hc,ct,hc
    29      12      17      15      18  # hc,ct,os1
    30      22      18      19      21  # os1,c,n_1
    31      20      20      19      18  # o,c,os1
    32       8      23      21      19  # ct,n_1,c
    33      19      19      21      22  # c,n_1,h
    34      21      20      19      21  # o,c,n_1
    35       4      26      23      21  # ct,ct,n_1
    36      13      24      23      21  # hc,ct,n_1
    37      13      25      23      21  # hc,ct,n_1
    38       9      23      21      22  # ct,n_1,h
    39       1      23      26      35  # ct,ct,ct
    40       1      23      26      27  # ct,ct,ct
    41       1      23      26      31  # ct,ct,ct
    42       2      26      23      24  # ct,ct,hc
```

```
43      10      24      23      25  # hc,ct,hc
44       2      26      23      25  # ct,ct,hc
45       1      26      35      38  # ct,ct,ct
46       2      26      35      36  # ct,ct,hc
47       2      26      35      37  # ct,ct,hc
48       2      26      27      28  # ct,ct,hc
49       2      26      27      29  # ct,ct,hc
50       2      26      27      30  # ct,ct,hc
51       2      26      31      32  # ct,ct,hc
52       2      26      31      33  # ct,ct,hc
53       2      26      31      34  # ct,ct,hc
54       1      27      26      35  # ct,ct,ct
55       1      27      26      31  # ct,ct,ct
56      10      28      27      29  # hc,ct,hc
57      10      28      27      30  # hc,ct,hc
58      10      29      27      30  # hc,ct,hc
59       1      31      26      35  # ct,ct,ct
60      10      32      31      33  # hc,ct,hc
61      10      32      31      34  # hc,ct,hc
62      10      33      31      34  # hc,ct,hc
63       1      35      38      44  # ct,ct,ct
64       1      35      38      40  # ct,ct,ct
65       2      35      38      39  # ct,ct,hc
66       2      38      35      36  # ct,ct,hc
67      10      36      35      37  # hc,ct,hc
68       2      38      35      37  # ct,ct,hc
69       1      38      44      47  # ct,ct,ct
70       2      38      44      45  # ct,ct,hc
71       2      38      44      46  # ct,ct,hc
72       2      38      40      41  # ct,ct,hc
73       2      38      40      42  # ct,ct,hc
74       2      38      40      43  # ct,ct,hc
75       2      44      38      39  # ct,ct,hc
76       2      40      38      39  # ct,ct,hc
77       1      40      38      44  # ct,ct,ct
78      10      41      40      42  # hc,ct,hc
79      10      41      40      43  # hc,ct,hc
80      10      42      40      43  # hc,ct,hc
81       4      44      47      50  # ct,ct,n_1
82       2      44      47      48  # ct,ct,hc
83       2      44      47      49  # ct,ct,hc
84       2      47      44      45  # ct,ct,hc
85      10      45      44      46  # hc,ct,hc
86       2      47      44      46  # ct,ct,hc
87       8      47      50      52  # ct,n_1,c
```

```
        88       9      47      50      51  # ct,n_1,h
        89      13      48      47      50  # hc,ct,n_1
        90      10      48      47      49  # hc,ct,hc
        91      13      49      47      50  # hc,ct,n_1
        92      22      54      52      50  # os1,c,n_1
        93      21      53      52      50  # o,c,n_1
        94      19      52      50      51  # c,n_1,h
        95       7      55      54      52  # ct,os1,c
        96      20      53      52      54  # o,c,os1
        97       3      58      55      54  # ct,ct,os1
        98      12      56      55      54  # hc,ct,os1
        99      12      57      55      54  # hc,ct,os1
       100       3      55      58      61  # ct,ct,os1
       101       2      55      58      59  # ct,ct,hc
       102       2      55      58      60  # ct,ct,hc
       103       2      58      55      56  # ct,ct,hc
       104      10      56      55      57  # hc,ct,hc
       105       2      58      55      57  # ct,ct,hc
       106       7      58      61      62  # ct,os1,c
       107      12      59      58      61  # hc,ct,os1
       108      10      59      58      60  # hc,ct,hc
       109      12      60      58      61  # hc,ct,os1
       110      17      64      62      61  # cm,c,os1
       111      20      63      62      61  # o,c,os1
       112      15      69      64      62  # cm,cm,c
       113       6      65      64      62  # ct,cm,c
       114      16      64      62      63  # cm,c,o
       115      14      64      69      70  # cm,cm,hc1
       116      14      64      69      71  # cm,cm,hc1
       117      11      66      65      64  # hc,ct,cm
       118      11      67      65      64  # hc,ct,cm
       119      11      68      65      64  # hc,ct,cm
       120       5      65      64      69  # ct,cm,cm
       121      10      66      65      67  # hc,ct,hc
       122      10      66      65      68  # hc,ct,hc
       123      10      67      65      68  # hc,ct,hc
       124      18      70      69      71  # hc1,cm,hc1

Dihedrals

         1       9       1       5       9      11  # ct,cm,c,os1
         2       8       1       5       9      10  # ct,cm,c,o
         3       7       1       5       6       7  # ct,cm,cm,hc1
         4       7       1       5       6       8  # ct,cm,cm,hc1
         5      19       2       1       5       9  # hc,ct,cm,c
```

```
 6      18       2       1       5       6  # hc,ct,cm,cm
 7      19       3       1       5       9  # hc,ct,cm,c
 8      18       3       1       5       6  # hc,ct,cm,cm
 9      19       4       1       5       9  # hc,ct,cm,c
10      18       4       1       5       6  # hc,ct,cm,cm
11      10      12      11       9       5  # ct,os1,c,cm
12      24       6       5       9      11  # cm,cm,c,os1
13      23       6       5       9      10  # cm,cm,c,o
14      25       7       6       5       9  # hc1,cm,cm,c
15      25       8       6       5       9  # hc1,cm,cm,c
16       4      15      12      11       9  # ct,ct,os1,c
17      20      13      12      11       9  # hc,ct,os1,c
18      20      14      12      11       9  # hc,ct,os1,c
19      11      12      11       9      10  # ct,os1,c,o
20      27      11      12      15      18  # os1,ct,ct,os1
21      16      16      15      12      11  # hc,ct,ct,os1
22      16      17      15      12      11  # hc,ct,ct,os1
23       4      12      15      18      19  # ct,ct,os1,c
24      16      13      12      15      18  # hc,ct,ct,os1
25      15      13      12      15      16  # hc,ct,ct,hc
26      15      13      12      15      17  # hc,ct,ct,hc
27      16      14      12      15      18  # hc,ct,ct,os1
28      15      14      12      15      16  # hc,ct,ct,hc
29      15      14      12      15      17  # hc,ct,ct,hc
30      12      15      18      19      21  # ct,os1,c,n_1
31      11      15      18      19      20  # ct,os1,c,o
32      20      16      15      18      19  # hc,ct,os1,c
33      20      17      15      18      19  # hc,ct,os1,c
34      14      23      21      19      18  # ct,n_1,c,os1
35      28      18      19      21      22  # os1,c,n_1,h
36       5      26      23      21      19  # ct,ct,n_1,c
37      21      24      23      21      19  # hc,ct,n_1,c
38      21      25      23      21      19  # hc,ct,n_1,c
39      13      23      21      19      20  # ct,n_1,c,o
40      26      20      19      21      22  # o,c,n_1,h
41       3      35      26      23      21  # ct,ct,ct,n_1
42       3      27      26      23      21  # ct,ct,ct,n_1
43       3      31      26      23      21  # ct,ct,ct,n_1
44       6      26      23      21      22  # ct,ct,n_1,h
45      22      24      23      21      22  # hc,ct,n_1,h
46      22      25      23      21      22  # hc,ct,n_1,h
47       1      23      26      35      38  # ct,ct,ct,ct
48       2      23      26      35      36  # ct,ct,ct,hc
49       2      23      26      35      37  # ct,ct,ct,hc
50       2      23      26      27      28  # ct,ct,ct,hc
```

```
51      2       23      26      27      29  # ct,ct,ct,hc
52      2       23      26      27      30  # ct,ct,ct,hc
53      2       23      26      31      32  # ct,ct,ct,hc
54      2       23      26      31      33  # ct,ct,ct,hc
55      2       23      26      31      34  # ct,ct,ct,hc
56      2       35      26      23      24  # ct,ct,ct,hc
57      2       27      26      23      24  # ct,ct,ct,hc
58      2       31      26      23      24  # ct,ct,ct,hc
59      2       35      26      23      25  # ct,ct,ct,hc
60      2       27      26      23      25  # ct,ct,ct,hc
61      2       31      26      23      25  # ct,ct,ct,hc
62      1       26      35      38      44  # ct,ct,ct,ct
63      1       26      35      38      40  # ct,ct,ct,ct
64      2       26      35      38      39  # ct,ct,ct,hc
65      1       27      26      35      38  # ct,ct,ct,ct
66      2       27      26      35      36  # ct,ct,ct,hc
67      2       27      26      35      37  # ct,ct,ct,hc
68      2       27      26      31      32  # ct,ct,ct,hc
69      2       27      26      31      33  # ct,ct,ct,hc
70      2       27      26      31      34  # ct,ct,ct,hc
71      2       35      26      27      28  # ct,ct,ct,hc
72      2       31      26      27      28  # ct,ct,ct,hc
73      2       35      26      27      29  # ct,ct,ct,hc
74      2       31      26      27      29  # ct,ct,ct,hc
75      2       35      26      27      30  # ct,ct,ct,hc
76      2       31      26      27      30  # ct,ct,ct,hc
77      1       31      26      35      38  # ct,ct,ct,ct
78      2       31      26      35      36  # ct,ct,ct,hc
79      2       31      26      35      37  # ct,ct,ct,hc
80      2       35      26      31      32  # ct,ct,ct,hc
81      2       35      26      31      33  # ct,ct,ct,hc
82      2       35      26      31      34  # ct,ct,ct,hc
83      1       35      38      44      47  # ct,ct,ct,ct
84      2       35      38      44      45  # ct,ct,ct,hc
85      2       35      38      44      46  # ct,ct,ct,hc
86      2       35      38      40      41  # ct,ct,ct,hc
87      2       35      38      40      42  # ct,ct,ct,hc
88      2       35      38      40      43  # ct,ct,ct,hc
89      2       44      38      35      36  # ct,ct,ct,hc
90      2       40      38      35      36  # ct,ct,ct,hc
91     15       36      35      38      39  # hc,ct,ct,hc
92      2       44      38      35      37  # ct,ct,ct,hc
93      2       40      38      35      37  # ct,ct,ct,hc
94     15       37      35      38      39  # hc,ct,ct,hc
95      3       38      44      47      50  # ct,ct,ct,n_1
```

```
 96      2      38      44      47      48  # ct,ct,ct,hc
 97      2      38      44      47      49  # ct,ct,ct,hc
 98      2      47      44      38      39  # ct,ct,ct,hc
 99     15      39      38      44      45  # hc,ct,ct,hc
100     15      39      38      44      46  # hc,ct,ct,hc
101     15      39      38      40      41  # hc,ct,ct,hc
102     15      39      38      40      42  # hc,ct,ct,hc
103     15      39      38      40      43  # hc,ct,ct,hc
104      1      40      38      44      47  # ct,ct,ct,ct
105      2      40      38      44      45  # ct,ct,ct,hc
106      2      40      38      44      46  # ct,ct,ct,hc
107      2      44      38      40      41  # ct,ct,ct,hc
108      2      44      38      40      42  # ct,ct,ct,hc
109      2      44      38      40      43  # ct,ct,ct,hc
110      5      44      47      50      52  # ct,ct,n_1,c
111      6      44      47      50      51  # ct,ct,n_1,h
112     17      45      44      47      50  # hc,ct,ct,n_1
113     15      45      44      47      48  # hc,ct,ct,hc
114     15      45      44      47      49  # hc,ct,ct,hc
115     17      46      44      47      50  # hc,ct,ct,n_1
116     15      46      44      47      48  # hc,ct,ct,hc
117     15      46      44      47      49  # hc,ct,ct,hc
118     14      47      50      52      54  # ct,n_1,c,os1
119     13      47      50      52      53  # ct,n_1,c,o
120     21      48      47      50      52  # hc,ct,n_1,c
121     22      48      47      50      51  # hc,ct,n_1,h
122     21      49      47      50      52  # hc,ct,n_1,c
123     22      49      47      50      51  # hc,ct,n_1,h
124     12      55      54      52      50  # ct,os1,c,n_1
125     28      54      52      50      51  # os1,c,n_1,h
126     26      53      52      50      51  # o,c,n_1,h
127      4      58      55      54      52  # ct,ct,os1,c
128     20      56      55      54      52  # hc,ct,os1,c
129     20      57      55      54      52  # hc,ct,os1,c
130     11      55      54      52      53  # ct,os1,c,o
131     27      54      55      58      61  # os1,ct,ct,os1
132     16      59      58      55      54  # hc,ct,ct,os1
133     16      60      58      55      54  # hc,ct,ct,os1
134      4      55      58      61      62  # ct,ct,os1,c
135     16      56      55      58      61  # hc,ct,ct,os1
136     15      56      55      58      59  # hc,ct,ct,hc
137     15      56      55      58      60  # hc,ct,ct,hc
138     16      57      55      58      61  # hc,ct,ct,os1
139     15      57      55      58      59  # hc,ct,ct,hc
140     15      57      55      58      60  # hc,ct,ct,hc
```

```
141      10      58      61      62      64  # ct,os1,c,cm
142      11      58      61      62      63  # ct,os1,c,o
143      20      59      58      61      62  # hc,ct,os1,c
144      20      60      58      61      62  # hc,ct,os1,c
145      24      69      64      62      61  # cm,cm,c,os1
146       9      65      64      62      61  # ct,cm,c,os1
147      25      70      69      64      62  # hc1,cm,cm,c
148      25      71      69      64      62  # hc1,cm,cm,c
149      19      66      65      64      62  # hc,ct,cm,c
150      19      67      65      64      62  # hc,ct,cm,c
151      19      68      65      64      62  # hc,ct,cm,c
152      23      69      64      62      63  # cm,cm,c,o
153       8      65      64      62      63  # ct,cm,c,o
154       7      65      64      69      70  # ct,cm,cm,hc1
155       7      65      64      69      71  # ct,cm,cm,hc1
156      18      66      65      64      69  # hc,ct,cm,cm
157      18      67      65      64      69  # hc,ct,cm,cm
158      18      68      65      64      69  # hc,ct,cm,cm
```

DISTRIBUTION:

1	MS 0886	T. J. Alam, 1853
1	MS 1314	D. S. Bolintineanu, 1516
1	MS 1411	M. C. Celina, 1853
1	MS 0889	J. M. D. Lane, 1814
1	MS 0888	J. R. McElhanon, 1853
1	MS 1411	E. M. Redline, 1853
1	MS 1315	M. J. Stevens, 1814
1	MS 0359	D. Chavez, LDRD Office, 1911
1	MS 0899	Technical Library, 9536 (electronic copy)


Sandia National Laboratories